FEBRUARY 2019 Ph.D. in Electrical and Electronics Engineering MEHMET DEMİR

REPUBLIC OF TURKEY

GAZİANTEP UNIVERSITY

GRADUATE SCHOOL OF

NATURAL & APPLIED SCIENCES

A NEW APPROACH FOR ONE-BIT COMPRESSED SYNTHETIC APERTURE RADAR IMAGING

Ph.D. THESIS

IN

ELECTRICAL AND ELECTRONICS ENGINEERING

BY

MEHMET DEMİR

FEBRUARY 2019

A New Approach for One-Bit Compressed Synthetic Aperture Radar Imaging

Ph.D. Thesis
in
Electrical and Electronics Engineering
Gaziantep University

Supervisor
Prof. Dr. Ergun ERÇELEBİ

By
Mehmet DEMİR

February 2019

REPUBLIC OF TURKEY
GAZİANTEP UNIVERSITY
GRADUATE SCHOOL OF
NATURAL AND APPLIED SCIENCES
ELECTRICAL AND ELECTRONICS ENGINEERING

Name of the Thesis	:	A New Approach for One-Bit Compressed Synthetic Aperture Radar Imaging
Name of the Student	:	Mehmet DEMİR
Exam Date	:	01.02.2019

Approval of the Graduate School of Natural and Applied Sciences.

Prof. Dr. Ahmet Necmeddin YAZICI
Director

I certify that this thesis satisfies all the requirements as a thesis for the degree of Doctor of Philosophy.

Prof. Dr. Ergun ERÇELEBİ
Head of Department

This is to certify that we have read this thesis and that in our opinion it is fully adequate, in scope and quality, as a thesis for the degree of Doctor of Philosophy.

Prof. Dr. Ergun ERÇELEBİ
Supervisor

Examining Committee Members:	Signature
Prof. Dr. Fatih Vehbi ÇELEBİ	....
Prof. Dr. Ergun ERÇELEBİ	....
Prof. Dr. Nuran DOĞRU	....
Asst. Prof. Dr. Kadir Sercan BAYRAM	....
Asst. Prof. Dr. Tolgay KARA	....

I hereby declare that all information in this document has been obtained and presented in accordance with academic rules and ethical conduct. I also declare that, as required by these rules and conduct, I have fully cited and referenced all material and results that are not original to this work.

Mehmet DEMİR

ABSTRACT

A NEW APPROACH FOR ONE-BIT COMPRESSED SYNTHETIC APERTURE RADAR IMAGING

DEMİR, Mehmet

Ph.D. in Electrical and Electronics Engineering

Supervisor: Prof. Dr. Ergun ERÇELEBİ

February 2019

74 pages

Synthetic Aperture Radar (SAR) imaging system requires too much measurements to achieve a high-resolution image. This situation also raises the need for fast analogue-to-digital-converters and large on board storage systems due to the large number of measurements. Using 1-bit quantization may be a rational solution to these issues. A new framework is introduced for 1-bit compressed SAR imaging by using time-varying thresholds in this dissertation. It has been demonstrated how to reconstruct sparse SAR images from noisy measurements which are quantized to 1-bit with time-varying thresholds. In conventional 1-bit Compressive Sensing (CS) algorithms 1-bit quantization has been done by comparing measurements to a zero threshold. This makes the magnitude information of the signal to be lost and exact signal recovery becomes impossible. Unlike those algorithms, we do 1-bit quantization by comparing the received signal to time-varying thresholds. With this 1-bit quantization method, unit-norm constraint, consistency function and sophisticated optimization algorithms are no longer needed. Moreover, the amplitudes of the signals obtained by this method are more accurate. Using this 1-bit quantization approach, we can formulate 1-bit CS SAR imaging reconstruction problem as an unconstrained optimization problem where the objective function includes ℓ_2 data-fidelity term and a non-smooth regularization function. For solving this unconstrained optimization problem, we use variable splitting and the alternating direction method of multipliers which is computationally efficient and easy to implement. The results from simulations with real and synthetic SAR images validate the effectiveness of the proposed algorithm named as BCST-SAR (Binary CS with Time-varying thresholds in SAR imaging).

Key words: Synthetic aperture radar, compressive sensing, 1-bit quantization, time-varying thresholds.

ÖZET

BİR-BİT SIKIŞTIRILMIŞ SENTETİK AÇIKLIKLI RADAR GÖRÜNTÜLEME İÇİN YENİ BİR YAKLAŞIM

DEMİR, Mehmet

Doktora Tezi, Elektrik ve Elektronik Mühendisliği Bölümü

Tez Yöneticisi: Prof. Dr. Ergun ERÇELEBİ

Şubat 2019

74 sayfa

Sentetik Açıklıklı Radar (SAR) görüntüleme sistemi, yüksek çözünürlüklü bir görüntü elde etmek için çok fazla ölçüm gerektirir. Bu durum aynı zamanda ölçüm sayısının çok fazla olmasından dolayı, hızlı analog-dijital dönüştürücülere ve büyük yerleşik depolama sistemlerine duyulan ihtiyacı da arttırır. 1-bit nicemlemeyi kullanmak, bu sorunlara rasyonel bir çözüm olabilir. Bu tezde zamanla değişen eşikler kullanılarak 1-bit sıkıştırılmış SAR görüntüleme için yeni bir çerçeve sunulmuştur. Seyrek SAR görüntülerinin zamana göre değişen eşik değerlerle 1-bit olarak ölçülen gürültülü ölçümlerden nasıl yeniden yapılandırılacağı gösterilmiştir. Geleneksel 1-bit Sıkıştırılmış Algılama (SA) algoritmalarında, ölçümleri sıfır eşik ile karşılaştırarak 1-bit nicemleme yapılmıştır. Bu, sinyalin büyüklüğünün kaybolmasına neden olur ve tam sinyal geri kazanımı imkansız hale gelir. Bu algoritmaların aksine, biz alınan sinyali zamanla değişen eşiklerle karşılaştırarak 1-bitlik nicemleme yapıyoruz. Bu 1-bitlik nicemleme metodu ile birim norm kısıtlaması, tutarlılık fonksiyonu ve sofistike optimizasyon algoritmaları artık gerekli değildir. Ayrıca, bu yöntemle elde edilen sinyallerin genlikleri daha doğrudur. Bu 1-bit nicemleme yaklaşımını kullanarak, 1-bit CS SAR görüntüleme yeniden yapılandırma problemini, amaç fonksiyonunun ℓ_2 veri doğruluğu terimi ve düzgün olmayan bir normalleştirme fonksiyonu içeren kısıtlanmamış bir optimizasyon sorunu olarak formüle edebiliriz. Bu kısıtlanmamış optimizasyon problemini çözmek için, değişken bölme ve hesaplama açısından verimli ve uygulaması kolay çarpanların alternatif yön yöntemini kullanıyoruz. Gerçek ve sentetik SAR görüntüleri içeren simülasyonlardan elde edilen sonuçlar, BCST-SAR (SAR görüntülemede zamanla değişen eşiklerle ikili SA) olarak adlandırılan, önerilen algoritmanın etkinliğini doğrulamaktadır.

Anahtar kelimeler: Sentetik açıklıklı radar, sıkıştırılmış algılama, 1-bit niceleme, zamanla değişen eşikler.

I dedicate this work to my family

ACKNOWLEDGEMENTS

First and foremost, I would like to thank the Most Merciful Allah for giving me the strength to complete this study.

I would like to express my deepest gratitude to my supervisor, Prof.Dr. Ergun ERÇELEBİ for his excellent guidance, caring, patience and insight throughout this study.

I would also thank to my deceased father Ali DEMİR. He always supported and encouraged me with his best wishes. I would like express my appreciation to my mother Edibe DEMİR who has had a lot of efforts in coming to this day.

I would also thank to my beloved daughter Belinay, who is the source of my life's happiness.

Finally, I would like to thank my wife Tuğba for her support and patience during all my studies.

TABLE OF CONTENTS

LIST OF TABLES

LIST OF FIGURES

LIST OF SYMBOLS

SAR : Synthetic Aperture Radar

ADC : Analogue-to-Digital Converter

CS : Compressive Sensing

PFA : Polar Format Algorithm

BP : Backprojection

BIHT : Binary Iterative Hard Thresholding

MSP : Matching Sign Pursuit

RFPI : Renormalized Fixed-Point Iteration

RSS : Restricted Step Shrinkage

AOP : Adaptive Outlier Pursuit

NARFPI : Noise-Adaptive RFPI

MAP : Maximum A Posteriori

RDA : Range Doppler Algorithm

ADMM : Alternating Direction Method of Multipliers

BCST-SAR : Binary CS with Time-varying Thresholds in SAR imaging

LFM : Linear Frequency Modulated

FFT : Fast Fourier Transform

RIP : Restricted Isometry Property

SPG : Spectral Projected Gradient

pSNR : peak-Signal-to-Noise Ratio

MSE : Mean-Square-Error

TBR : Target-to-Background Ratio

CHAPTER 1

INTRODUCTION TO SYNTHETIC APERTURE RADAR

This dissertation presents a new framework for 1-bit compressed synthetic aperture radar image reconstruction problem. 1-bit quantisation has very important benefits in Synthetic Aperture Radar (SAR) imaging whose popularity has increased in recent years. SAR system needs large amount of measurements to produce high-resolution images and therefore fast Analogue-to-Digital Converters (ADC) are necessary. 1-bit quantisation is used for SAR imaging because of its rapidity. This chapter discusses the following topics: 1) describes what SAR imaging is and in what situations it can be useful; 2) explains the SAR imaging modes and mention about which classical reconstruction algorithms are used for each mode; 3) gives literature survey associated with 1-bit SAR imaging and 1-bit Compressive Sensing, then explains how this thesis contributes to the 1-bit SAR imaging problem; 4) presents the outline of the thesis.

1.1 Synthetic Aperture Radar Imaging

SAR is a high-resolution imaging system for capturing two-dimensional image of earth's surface at night and in all adverse weather conditions that cannot be imaged by Electro-optical and Infrared cameras. The ability to perform imaging in very adverse weather conditions is the most important feature of SAR because it uses its own illumination. The SAR sensor can either be mounted on an airplane or on a satellite in orbit depending on its intended use. SAR systems are widely used for military and civilian applications. In military applications, its main use is intelligence, reconnaissance and surveillance. On the other hand, it is also used in civilian applications such as topographical mapping, oil spill detection and forest resource analysis, etc[1]. For example, a SAR image obtained from SIR-C/X is displayed in Figure 1.1[2].

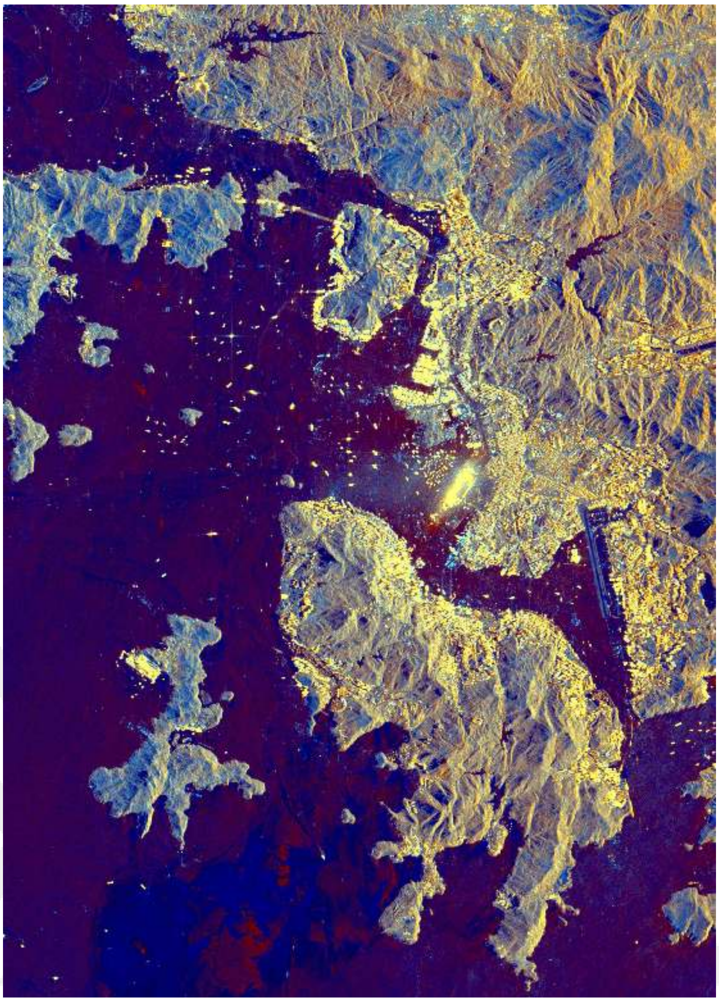

Figure 1.1 An example of SIR-C/X-SAR image[2].

The SAR sensor carried on the airplane or on the satellite platforms follows a path and transmits microwave pulses toward the ground at certain intervals along this path, as illustrated in Figure 1.2. When performing SAR imaging, it is of utmost importance to calculate the exact position of the platform carrying the sensor with respect to the imaged ground area. Microwave radar signals are sent to the area of interest to be imaged and the return echoes are processed to generate SAR image. The received signal first passes through a pre-processing and then image formation processor is made use of to obtain SAR image. The resolution in SAR imaging is independent of the distance between sensor and the target region of interest. For SAR systems, it is necessary to make improvements on the radar device itself to obtain precise and quality images. In this sense, resolution is very important. Achieving a high resolution image is related to transmitting a high-frequency, high-bandwidth signal. Roughly, typical SAR system consists of the steps illustrated in Figure 1.3.

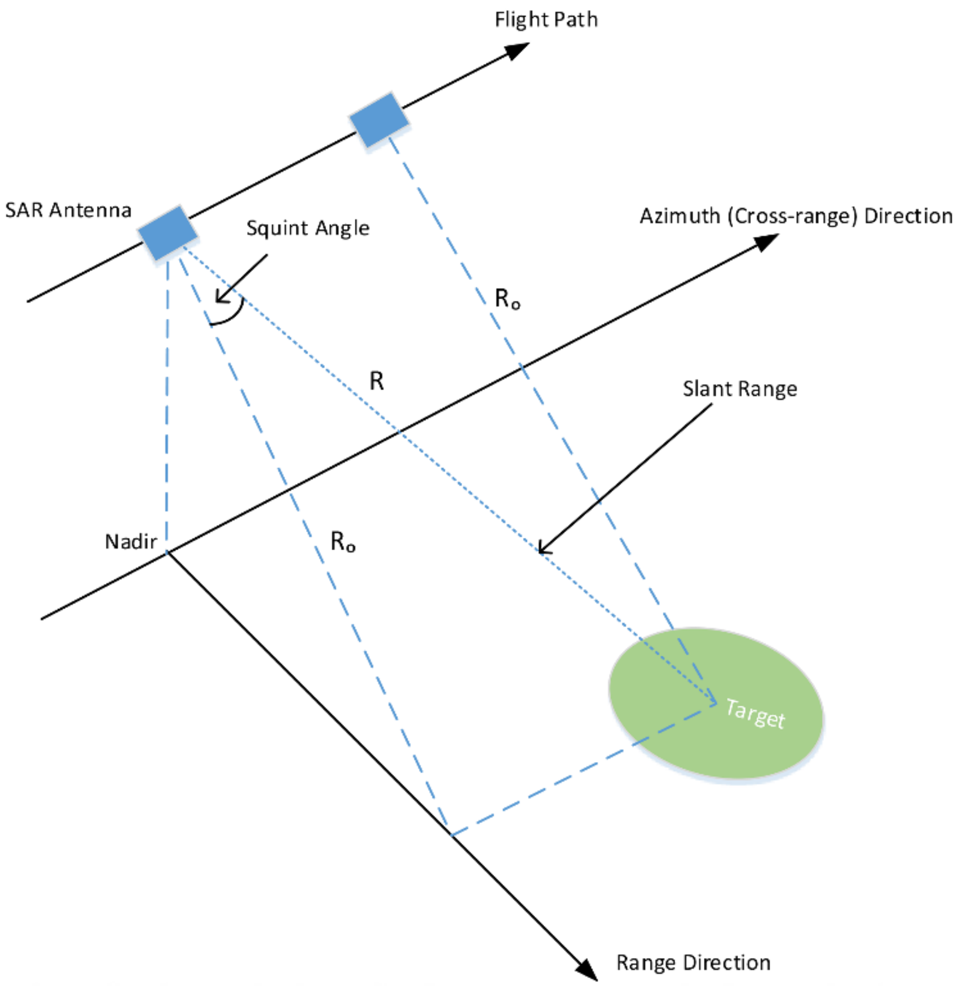

Figure 1.2 Simple illustration of SAR imaging system.

Figure 1.3 Stages of SAR system.

Some of the analogue signal transmitted toward the ground is reflected back to the sensor. The received signal is first down-converted and then is sampled at the Nyquist rate using ADC in a conventional SAR system. The sampling rate of ADC is completely dependent upon the bandwidth of transmitted SAR signal which determines the range resolution. The raw SAR data, sampled and stored in memory, is sent to the image formation processor where a SAR image is reconstructed.

Range resolution is conditional on the bandwidth of the transmitted signal. In case the bandwidth is increased in SAR system, the range resolution of SAR image becomes higher. Azimuth (cross-range) resolution depends on the length of synthetic aperture. Longer aperture means that finer azimuth resolution.

1.2 Modes of Synthetic Aperture Radar

The are two main imaging modes in SAR system. These modes are stripmap and spotlight. In stripmap mode as shown in Figure 1.4, the angle of SAR antenna does not change with respect to flight route as the platform moves, so the angle of antenna is always kept constant according to the imaged region. This mode is used for strip image of large scenes with coarser resolution[1].

In spotlight-mode SAR imaging, as the platform carrying on the SAR antenna progresses, SAR sensor directs its antenna beam to the ground area to be continuously imaged. So the angle of antenna is not constant and changes at each data collection interval. Spotlight-mode is utilised for imaging of relatively small areas with high-resolutions. Spotlight-mode produces higher-resolution images than stripmap-mode does. Spotlight-mode SAR geometry is shown in Figure 1.5. When the SAR system is used for military applications, a general view of the terrain is created with the stripmap mode, then the resulting image is scanned and the possible targets are determined. At the end, spotlight mode task is run for specified targets and a high resolution SAR image of the targets is created[1].

The data acquisition geometry of these two SAR modes is different as shown in Figures 1.4 and 1.5. In addition, these two modes may vary in terms of reconstruction algorithms. In stripmap mode, range-Doppler[3], chirp-scaling[4] and range-migration[5] algorithms can be used. In spotlight-mode SAR processing, Polar Format Algorithm (PFA)[6] and Backprojection (BP) algorithm[7, 8] are used predominantly. In addition to these algorithms, chirp-scaling and range-migration algorithms can also be used for spotlight SAR. Apart from these mentioned methods, Matched Filter (MF)[8] method is also made use of both SAR imaging modes. In this thesis, we focus on spotlight-mode SAR imaging.

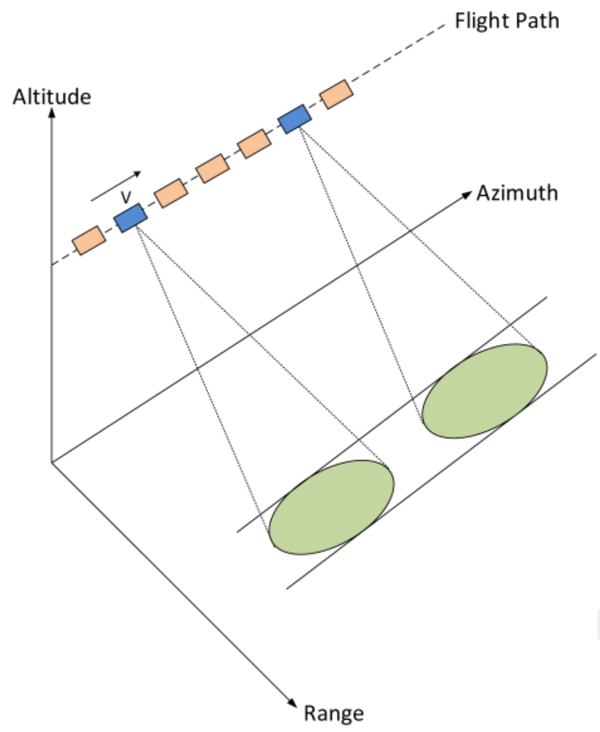

Figure 1.4 Stripmap mode SAR.

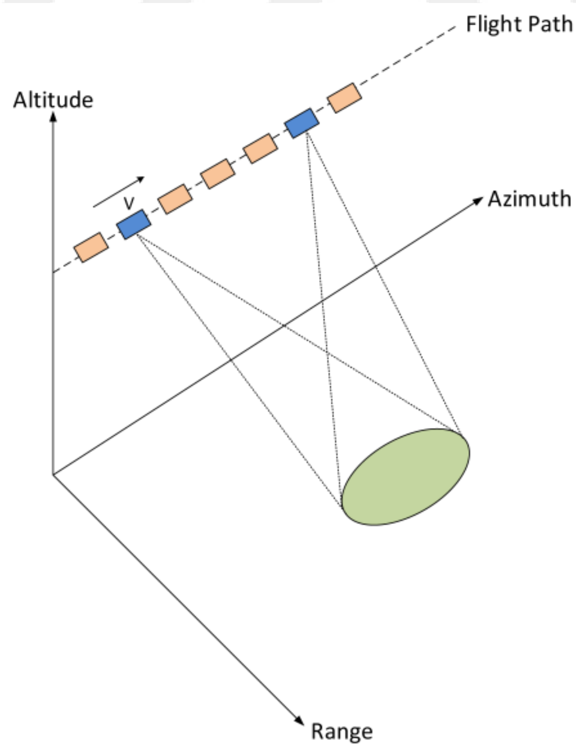

Figure 1.5 Spotlight mode SAR.

1.3 Review of 1-bit SAR Imaging Algorithms and the Contributions of the Dissertation

The SAR system used in situations where optical imaging systems are inadequate requires too much measurements to obtain high resolution images. This increases the need for a high-speed ADC and a large on-board storage system. Using low-bit quantisation in the SAR system to get rid of this heavy burden can be a rational solution. In this thesis, 1-bit quantisation which is the extreme case of low-bit quantisation has been used for spotlight mode SAR imaging. It is not a new application in SAR imaging. There have been some implementations of 1-bit quantisation of SAR in the past. In [9–11], the theory of 1-bit coded SAR signals together with numerical experiments on both simulated and real data has been investigated in great detail. In [12], a complete theory of SAR imaging from phase-only data has been studied for low-bit coded raw signal.

1-bit quantisation has significant advantages. Its ability to provide a fast sampling rate with low cost and low energy consumption is its main advantage. Also, it is robust to nonlinear distortions, saturations and other errors. 1-bit quantisation provides significant benefits, especially in large-bandwidth systems. On the other hand, 1-bit quantisation produces ghost targets in SAR imaging[10]. This is the biggest drawback of it in SAR imaging. It has been shown that ghost targets disappear at low Signal-to-Noise Ratio (SNR) situations[13, 14]. However, in this case the quality of SAR image itself is deteriorating. In our work, we tried to do spotlight SAR imaging with 1-bit quantisation without degrading the quality of the image itself.

In recent years, a new theory has emerged that allows signal acquisition below the Nyquist rate. This theory is called Compressive Sensing (CS)[15, 16]. This framework makes it possible to reconstruct sparse signals from highly incomplete random measurements. There are many applications of this theory in SAR signal processing[17, 18]. In conventional CS framework, it is assumed that measurements have infinite bit precision. But in practice, measurements have to be quantised in order to operate with digital hardware. In order to make easier the practical implementation of CS, the effect of quantised measurements on CS has been searched by Zymnis, Boyd and Candès[19]. Furthermore, 1-bit CS has also been studied. 1-bit in CS is first introduced by Boufonous and Baraniuk[20]. Later, it has been shown that stable signal reconstruction can be obtained from 1-bit measurements[21]. One-bit CS framework has drawn so much attention and many algorithms have been developed for the reconstruction from 1-bit measurements. To solve 1-bit CS problem, greedy algorithms called Binary Iterative Hard Thresholding (BIHT)[21], Matching Sign Pursuit (MSP)[22] are proposed. However, these algorithms require us to know the sparsity level of the signal in advance. To know the sparsity constant beforehand is so hard in practice. The Renormalized Fixed-Point Iteration (RFPI)[20] and Restricted Step Shrinkage (RSS)[23] algorithms, which are based on ℓ_1-norm minimization and do not need the sparsity level of the signal, have also been proposed.

In 1-bit quantisation, the noise in the signal can cause the sign flip. In order to overcome the sign flip, several algorithms such as Adaptive Outlier Pursuit (AOP)[24] and Noise-Adaptive RFPI (NARFPI)[25] algorithms have been introduced. The AOP algorithm, which is the improved version of the BIHT algorithm, also needs the sparsity level of the signal. Additionally, the number of sign flips is required for it. The NARFPI algorithm which combines the good aspects of the AOP and RFPI algorithms overcomes the sign flip and does not need the sparsity level of the signal. The optimisation problems in all of these aforementioned algorithms are nonconvex because a unit-norm constraint has to be imposed on the problem for nontrivial solution. The initialisation values should be carefully chosen in nonconvex optimization whereas convex optimisation has no such problems. Convex optimisation approaches for 1-bit CS have been suggested for approximately sparse signals[26, 27]. Bayesian-based approaches are also presented in addition to these methods for signal recovery in 1-bit CS[13, 28].

The reconstruction algorithms for 1-bit CS in SAR imaging have been demonstrated in [13, 14]. A Maximum A Posteriori (MAP) estimation approach is utilised to reconstruct the SAR image in [13]. The MAP approach uses the cumulative distribution function of the standard normal distribution to enforce the data consistency with estimates. This algorithm is very slow because Newton's method is employed in it. In [14], the authors have benefited from the sigmoid function and have used the Range-Doppler Algorithm (RDA) to reduce the computational complexity. The method which is presented in [14] is only suitable for the stripmap mode SAR whereas the MAP approach which is proposed in [13] can be used for both spotlight and stripmap modes SAR.

Many of the earlier studies in 1-bit CS consider the case where the signal is compared to a fixed threshold that is usually zero. In this case, the amplitude information of the signal is lost and only the sign information of the signal is retained. This makes it impossible to reconstruct the sparse signal precisely. The unit-norm constraint has to be imposed on the sparse signal in these early 1-bit CS methods to restore the signal, otherwise the algorithms can produce trivial all-zero solutions. To cope with unit-norm constraint, sophisticated optimisation methods[23], alternative constraints[26] or the functions that quantify the consistency between the measured 1-bit quantised data and the reconstructed signal[13, 14, 29] need to be used. However, some of the recent studies have proposed random time-varying thresholds[30–35] where 1-bit measurements are captured by comparing signals to time-varying threshold levels. Thus, the quantisation to 1-bit with properly chosen thresholds enables to recover the amplitude of the signal more accurately. In our study, 1-bit quantisation is performed via a comparator with time-varying thresholds and the unit-norm constraint or the consistency functions between the measurements and the estimates are no longer needed. The advantage of the proposed approach is that we can solve 1-bit CS SAR image reconstruction problem without using sophisticated optimisation techniques. We prefer to use variable splitting and the Alternating Direction Method of Multipliers (ADMM) to handle this optimisation problem because it is computationally efficient and bears a potential for parallel implementation.

Variable splitting and ADMM techniques have been successfully applied in compressed SAR image recovery problems[36, 37]. ADMM has yielded very good results when compared to the conventional methods in computational performance. It has enough computational efficiency to compete with greedy methods[37]. ADMM splits the unconstrained convex optimisation problem into sub-problems and achieves the general result by minimizing these sub-problems separately. Therefore, it gives fast results and is easy to implement. Because of this feature of ADMM, we aim at solving the 1-bit CS SAR imagery problem, which is 1-bit quantised with time-varying thresholds, by using variable splitting and ADMM technique. We name the proposed method as BCST-SAR (Binary CS with Time-varying thresholds in SAR imaging).

1.4 Organisation of the Thesis

In Chapter 2, basic mathematical model of spotlight-mode SAR imaging is presented. Range and azimuth resolution derivations of spotlight-mode SAR are given. Later, basics of CS are explained. It is described with examples at the end of Chapter 2 where conventional CS algorithms can not be used for 1-bit CS SAR imaging problems.

In Chapter 3, how to perform undersampling on compressed SAR imaging is discussed. Basic recovery algorithms of 1-bit CS problems are explained. Then, 1-bit quantization in CS SAR using time-varying thresholds is defined. At the end of chapter, ADMM algorithm and how to apply this algorithm to 1-bit CS SAR imaging are defined.

Chapter 4 is related to the validation of BCST-SAR algorithm with simulations. We give results obtained from the proposed method and compare it with the classical and state-of-the-art algorithms in this chapter. Some metrics are used for comparison of state-of-the-art algorithms in this chapter. Also the run-time comparisons of the proposed method with the other algorithms are presented.

Chapter 5 evaluates the simulation results and indicates potential future research areas.

CHAPTER 2

SPOTLIGHT SAR BASICS AND COMPRESSIVE SENSING

2.1 Mathematical Model of Spotlight-Mode SAR Imaging

In this thesis, we examine the imaging of spotlight-mode SAR in detail. Therefore, we have described the mathematical model of spotlight SAR. The ground-plane geometry of spotlight-mode SAR imaging is shown in Figure 2.2[39, 40]. The data are collected using radar pointing in a fixed ground patch as it travels along a flight path. High-bandwidth pulses are transmitted at the points corresponding to each increment of θ. The received signals returning from the ground patch are processed in order to form an image of the complex reflectivity field $f(x, y)$. Linear Frequency Modulated (LFM) chirp signals are usually used in spotlight-mode SAR. The mathematical formulation of the transmitted chirp signal is as follows:

$$\begin{cases} e^{j(\omega_0+\alpha t^2)}, & |t| \le \frac{\tau_c}{2} \\ 0, & otherwise \end{cases} \tag{2.1}$$

where ω_0 is the carrier frequency, 2α is the chirp rate, and τ_c is the pulse length of the transmitted signal. SAR sends the real part of LFM chirp signal at equidistant intervals as it travels in azimuth direction. The distance between SAR and the ground patch to be imaged is R_θ and it varies depending on the viewing angle θ. The convolution of the transmitted LFM chirp signal with the projection $q_\theta(u)$ of the imaging field at that aperture position gives the received signal $p_\theta(t)$ at the observation angle θ.

$$p_\theta(t) = Re\left\{\int q_\theta(u)exp\left\{j(\omega_0(t-\tau_0-\tau(u)) + \alpha(t-\tau_0-\tau(u))^2)\right\}du\right\} \quad (2.2)$$

$$q_\theta(u) = \iint\limits_{x^2+y^2\leq L^2} \delta(u - xcos\theta - ysin\theta)f(x,y)dxdy \quad (2.3)$$

where L is the spatial extent of the ground circular patch and $f(x,y)$ is the underlying field. τ_0 is called as demodulation time and equal to $\frac{2R}{c}$. The distance between SAR antenna and the target is shown in Figure 2.1. The delay time of the signal returned from target is $\tau_0 + \tau(u)$. The corresponding observation model of spotlight-mode SAR imaging can be seen in Figure 2.2. The received signals are first mixed with a reference chirp and then passed through a low-pass filter[41]. In-phase and quadrature versions of the transmitted LFM chirp signal are shown in (2.4) and (2.5). In-phase and quadrature reference chirps consist of cosine and sine functions. The signal that forms after multiplication is passed through a low-pass filter.

$$s_I(t) = cos(\omega(t-\tau_0) + \alpha(t-\tau_0)^2) \quad (2.4)$$

$$s_Q(t) = -sin(\omega(t-\tau_0) + \alpha(t-\tau_0)^2) \quad (2.5)$$

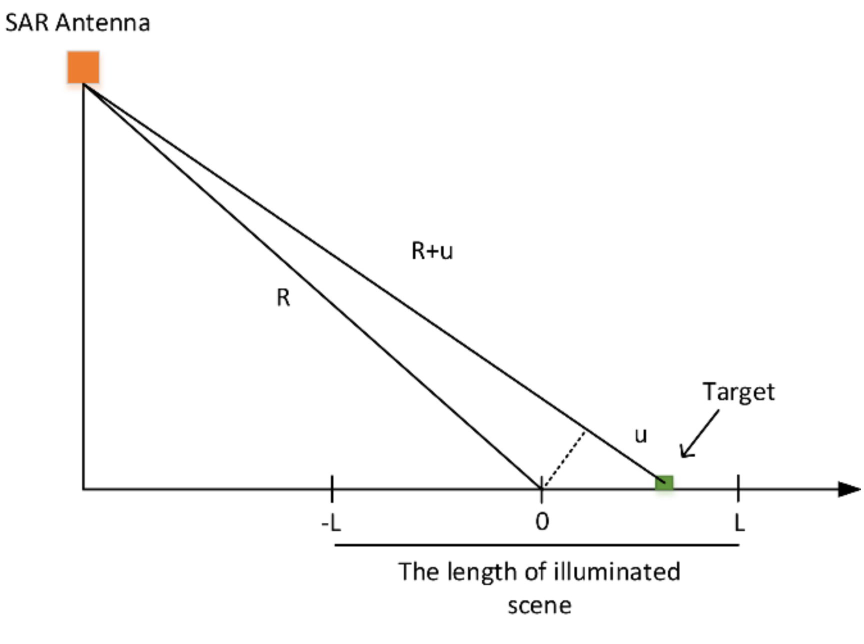

Figure 2.1 The length between SAR antenna and target[38].

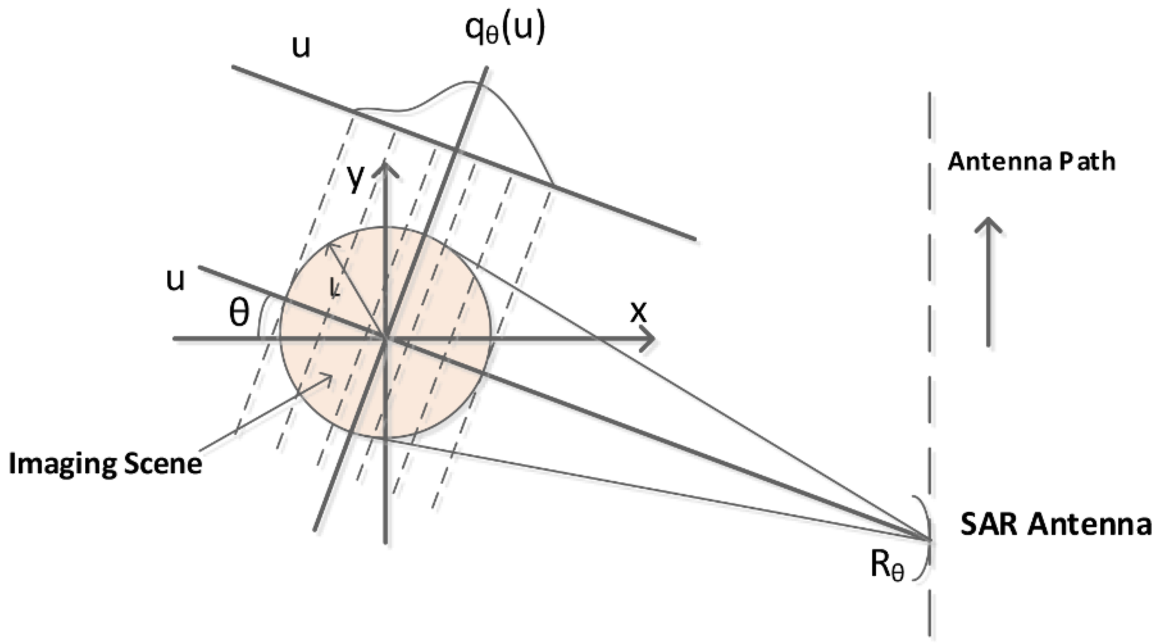

Figure 2.2 Ground-plane geometry of spotlight-mode SAR imaging[39, 40].

As the projection-slice theorem implies[42], the demodulated SAR signal $r_\theta(t)$ can be regarded as a band-pass filtered Fourier transform of the underlying field to be displayed after pre-processing step. The demodulated signal is given by

$$r_\theta(t) = \int\limits_{|u|\leq L} q_\theta(u) e^{-j\Omega(t)u} du \tag{2.6}$$

where $\Omega(t) = \frac{2}{c}(\omega_0 + 2\alpha(t - \frac{2R_\theta}{c}))$ is the radial spatial frequency. c is the speed of light. If we assume that $L \ll R_\theta$ the quadratic phase term which occurs after demodulation becomes very small and it can be neglected. If (2.3) is inserted into (2.6), we can see more clearly the relationship between the underlying field $f(x, y)$ and the demodulated SAR data $r_\theta(t)$ and obtain the following equation

$$r_\theta(t) = \iint\limits_{x^2+y^2\leq L^2} f(x, y) exp\left\{-j\Omega(t) \cdot (xcos\theta + ysin\theta)\right\} dxdy \tag{2.7}$$

The demodulated signals that are obtained from all viewing angles are two-dimensional spatial Fourier transform of the underlying field and form a patch. These demodulated signals can be called as phase histories. They lie on a polar-grid in the annulus segment as shown in Figure 2.3

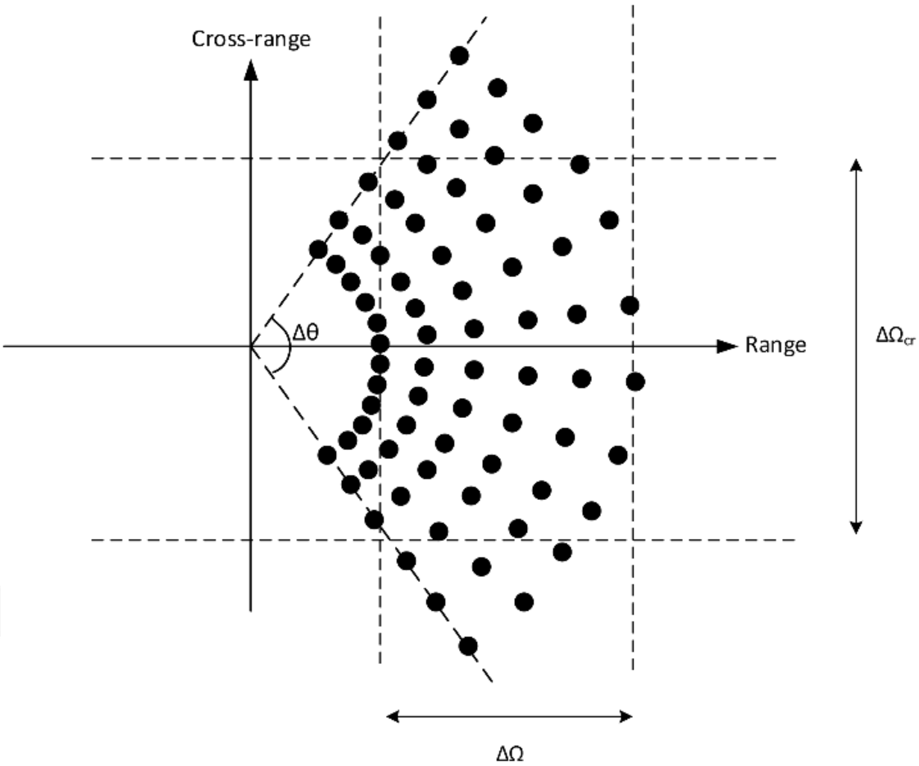

Figure 2.3 Representation of an annulus segment containing phase history data in two-dimensional frequency domain.

If imaging scene is discretized to get rid of the integral, the demodulated signal can also be expressed as follows:

$$r_\theta(t) = \sum_{k=1}^{K} f(x_k, y_k) exp\left\{-j\Omega(t) \cdot (x_k cos\theta + y_k sin\theta)\right\} + \epsilon(t) \tag{2.8}$$

where $k = 1, 2, ..., K$ includes all points containing the scatterers and $\epsilon(t)$ is additive white Gaussian noise. $f(x_k, y_k)$ is the complex-valued reflectivity function at all spatial locations (x_k, y_k). If we turn the unknown reflectivity field into a lexicographic vector, the demodulated signal can be written as:

$$r_\theta(t) = \mathbf{H}_\theta(t)\mathbf{f} + \epsilon(t) \tag{2.9}$$

where $\mathbf{H}_\theta$ is the discrete SAR projection operator at angle θ and $\mathbf{f}$ is the vectorized form of the two-dimensional underlying field.

2.1.1 Range and Azimuth Resolution

The returned signal at the demodulation step is considered to be within the following time interval:

$$\tau_0 - \frac{\tau_c}{2} + \frac{\tau_p}{2} \leq t \leq \tau_0 + \frac{\tau_c}{2} - \frac{\tau_p}{2} \tag{2.10}$$

where τ_c is the pulse duration of the transmitted LFM chirp signal. τ_p is the patch propagation time. The two-way propagation delay difference between target on the near edge and the target of the far-edge of the illuminated patch can be expressed as τ_p. For the duration of the return signal to be approximately equal to τ_c, the τ_p is intentionally selected much smaller than τ_c.

$$\tau_p \ll \tau_c \tag{2.11}$$

As seen in (2.10), the processed received signal is valid for the specific time interval. In this case, the Fourier transform of the underlying field can be determined over the range of the following spatial frequencies

$$\frac{2}{c}(\omega_0 - \alpha(\tau_c - \tau_p)) \leq \Omega \leq \frac{2}{c}(\omega_0 + \alpha(\tau_c - \tau_p)) \tag{2.12}$$

Since we assume $\tau_p \ll \tau_c$, the bandwidth of transmitted LFM chirp signal can be defined by

$$B_c = \frac{\alpha \tau_c}{\pi} \tag{2.13}$$

So the spatial frequency range of the phase history data in the range dimension can be written as following

$$\Delta\Omega \approx \frac{4\alpha\tau_c}{c} = \frac{4\pi B_c}{c} \tag{2.14}$$

In order to find the cross-range resolution, we can offer such an approach. The nominal cross-range limit of phase-history data is $\frac{4\pi}{\lambda_0}$ and the angular limit of the annulus segment is $\Delta\theta$. So, spatial frequency range of phase-history data in cross-range dimension can be given by

$$\Delta\Omega_{cr} = 2(\frac{4\pi}{\lambda_0})sin(\Delta\theta/2) \tag{2.15}$$

where $\lambda_0 = 2\pi c/\omega_0$. In spotlight-mode SAR imaging, $\Delta\theta$ is very small. In this case, $\Delta\Omega_{cr}$ can be approximated by

$$\Delta\Omega_{cr} \approx \frac{4\pi}{\lambda_0}\Delta\theta \tag{2.16}$$

After these expressions, range and cross-range resolutions can be obtained as follows:

$$\rho_r = \frac{2\pi}{\Delta\Omega} \approx \frac{c}{2B_c} \tag{2.17}$$

$$\rho_{cr} = \frac{2\pi}{\Delta\Omega_{cr}} \approx \frac{\lambda_0}{2\Delta\theta} \tag{2.18}$$

2.1.2 Conventional SAR Image Reconstruction Methods

In conventional spotlight-mode SAR image reconstruction, two algorithms PFA and BP are commonly used. As mentioned in the previous section, the demodulated SAR signal is the band-pass filtered Fourier transform of the underlying field. Therefore, PFA uses two-dimensional inverse Fourier transform to obtain the SAR image. Here, Fourier transform is carried out with fast Fourier transform (FFT) because it is fast. Before FFT in PFA algorithm, the SAR phase history data has to be interpolated from the polar grid to the Cartesian grid. PFA is a very advantageous method in terms of speed. On the other hand, BP uses one-dimensional FFT. In BP algorithm, one-dimensional interpolation is required after inverse FFT.

The MF method was applied conventionally in order to obtain the image from 1-bit quantised SAR data[9–12]. We also compared the results obtained from MF algorithm to measure whether the method we proposed is effective or not. FFT is not used in the MF method and to perform separate processing for each pixel to create the SAR image. For this reason, this algorithm is very slow[8]. However, in the literature it is not possible to apply the method other than MF to get SAR images from 1-bit quantised SAR data[9–12].

2.2 A Brief Review of Compressive Sensing

Compressive Sensing/Compressive Sampling (CS) is a signal processing technique that has emerged in recent years and provides significant advantages in the field of signal processing. This technique allows for reliable signal reconstruction from a set of under-determined linear measurements. The only condition in which CS can be applied is that the signal is sparse or compressible on the known transform basis $\mathbf{\Psi}$ (Wavelet, Curvelet, DCT, Fourier, etc)[43, 44]. Many signals that we encounter in nature are usually sparse in some transform basis. Therefore, the application area of CS is very wide. Examine the following linear measurement model

$$\mathbf{r} = \mathbf{H}\mathbf{f} \tag{2.19}$$

where $\mathbf{H} \in \mathbb{R}^{M \times N}$ is the measurement matrix, $\mathbf{r} \in \mathbb{R}^{M}$ is the measured signal and $\mathbf{f} \in \mathbb{R}^{N}$ is the unknown signal that is to be restored and can be represented sparsely in a known transform basis as follows

$$\mathbf{f} = \mathbf{\Psi}\mathbf{x} \tag{2.20}$$

The $\mathbf{x}$ vector consists of sparse representation coefficients. Replacing (2.20) into (2.19), the following result is obtained

$$\mathbf{r} = \mathbf{H}\mathbf{f} = \mathbf{H}\mathbf{\Psi}\mathbf{x} = \mathbf{A}\mathbf{x} \tag{2.21}$$

where $\mathbf{A} = \mathbf{H}\mathbf{\Psi}$ and $M \ll N$. The row number of matrix $\mathbf{A}$ is far fewer than the column number.

The linear under-determined system in (2.21) is ill-conditioned and we encounter such a system of equations in many signal processing problems, but if $\mathbf{x}$ is known to be sparse in this system of equation, the solution to this problem can be found. The following ℓ_0-norm minimization can be recommended to solve this linear system of equation (2.21)

$$\min \|\mathbf{x}\|_0 \quad \text{subject to} \quad \mathbf{r} = \mathbf{A}\mathbf{x} \tag{2.22}$$

where $\|\mathbf{x}\|_0$ is defined as the number of non-zero entries in $\mathbf{x}$. However, this

ℓ_0-norm problem is NP-Hard and combinatorially intractable. Donoho demonstrated that 2.22 is the same as the following ℓ_1-norm minimization problem if the measurement matrix complies with certain conditions[45]

$$\min \|\mathbf{x}\|_1 \quad \text{subject to} \quad \mathbf{r} = \mathbf{A}\mathbf{x} \tag{2.23}$$

This problem is also referred to as Basis Pursuit. There are many alternatives to solve this ℓ_1-norm minimization problem. For the solution of Basis Pursuit problem, methods such as greedy search algorithms[46], Bregman iterative regularization algorithm[47], a spectral gradient-projection method[48], etc. have been proposed in recent years.

In order for being able to recover a sparse signal successfully and stably from noisy measurements by solving 2.23, the matrix $\mathbf{A}$ has to satisfy the following Restricted Isometry Property (RIP)[49]

$$(1-\delta_s)\|\mathbf{x}\|_2^2 \leq \|\mathbf{A}\mathbf{x}\|_2^2 \leq (1+\delta_s)\|\mathbf{x}\|_2^2 \tag{2.24}$$

where isometry constant $0 \leq \delta_s < 1$ and $\|\mathbf{x}\|_0 < s$ (s is the sparsity level). Since it is very tedious to check whether any measurement matrix satisfies the RIP condition or not, it has been proven in the literature that Bernoulli, Gaussian and partial Fourier matrices provide the RIP property with high probability.

A Spectral Projected Gradient(SPGL1)[48] method is appropriate to solve conventional CS SAR imaging problems because this algorithm works in solving the problems which are in the complex domain. The SAR image reconstruction problem is also in the complex domain. However, as shown in Figures 2.4 and 2.5, this algorithm does not work in obtaining image from 1-bit quantized compressed SAR data. With this method, it is seen that it is very difficult to distinguish the target from images obtained from 1-bit quantized compressed SAR data. Because there is no 1-bit quantization constraint in the classical CS optimization problem, these algorithms do not perform well in 1-bit CS problems. Therefore, there must be extra constraints for 1-bit quantization in 1-bit CS SAR problems.

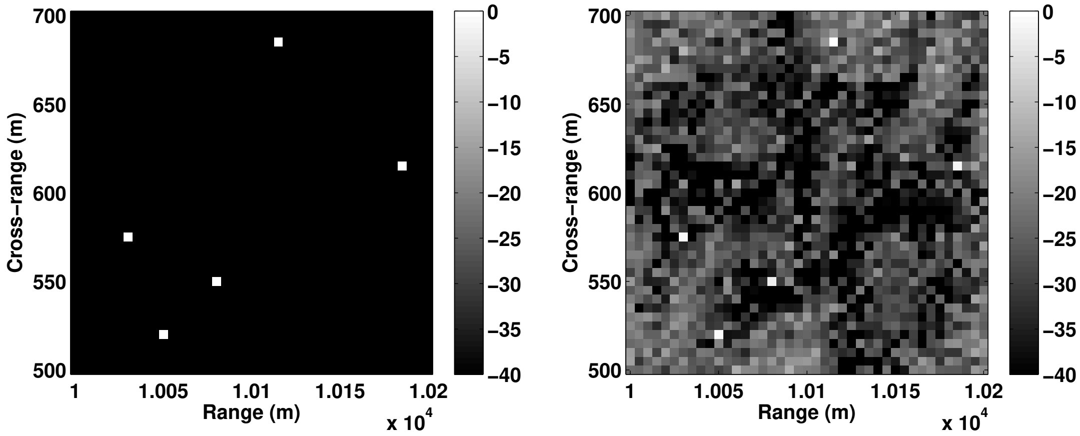

(a) Original scene. **(b)** 1-bit CS SAR using SPGL1.

Figure 2.4 Point Targets which are obtained using SPGL1 without and with 1-bit quantization.

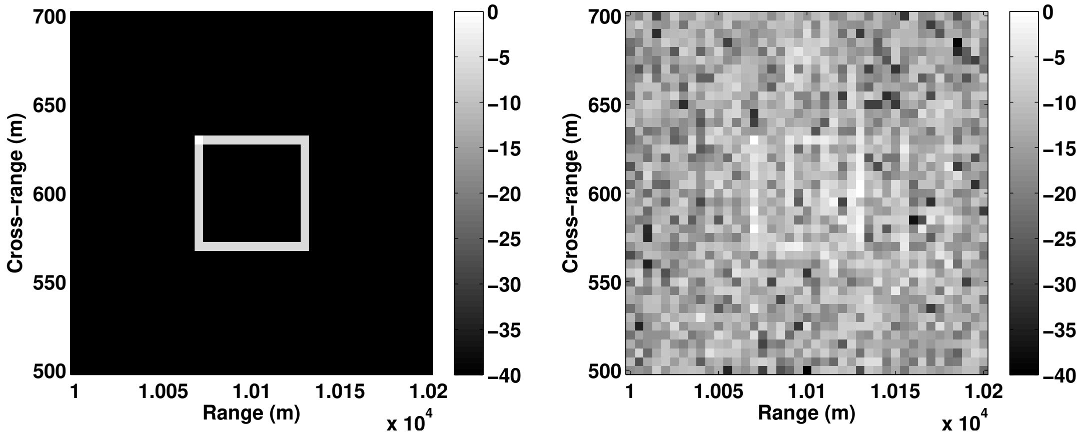

(a) Original scene. **(b)** 1-bit CS SAR using SPGL1.

Figure 2.5 Particular geometry scene which is obtained using SPGL1 without and with 1-bit quantization.

CHAPTER 3

ADMM BASED ONE-BIT COMPRESSIVE SENSING SAR

3.1 Undersampling Scheme in CS SAR

Conventional SAR imaging systems do not undergo any under-sampling as illustrated in Figure 3.1. In CS-based data acquisition systems, a random matrix is usually chosen to provide the RIP condition as the measurement matrix. Various methods have been proposed as under-sampling scheme in CS-based SAR imaging systems. The undersampling scheme is created either by random selection of only slow-time samples[18] or by random selection of both slow-time and fast-time samples[40, 43].

While SAR sensor is advancing along the flight path, LFM chirp pulses are transmitted and received at every Pulse Repetition Interval (PRI) where PRI=1/PRF (Pulse Repetition Frequency). Slow-time sampling is determined by PRF in classical SAR systems. The random undersampling in slow-time is generated by transmitting and receiving chirp pulses at random intervals rather than at traditional PRI. The random undersampling scheme in slow-time is shown in Figure 3.2.

The random undersampling scheme in fast and slow-time is produced by the use of non-uniform ADCs operating at a low sampling rate of the signals transmitted and received at randomly selected intervals. The random undersampling scheme in both fast-time and slow-time is demonstrated in Figure 3.3. The undersampling in slow-time reduces only the imaging time significantly, while the undersampling in both fast-time and slow-time reduces both the imaging time and the sampling rate. In this respect, the use of CS in SAR imaging provides significant advantages. In our work, CS under-sampling scheme for SAR imaging is formed by choosing slow-time and fast-time samples randomly as in the latter case.

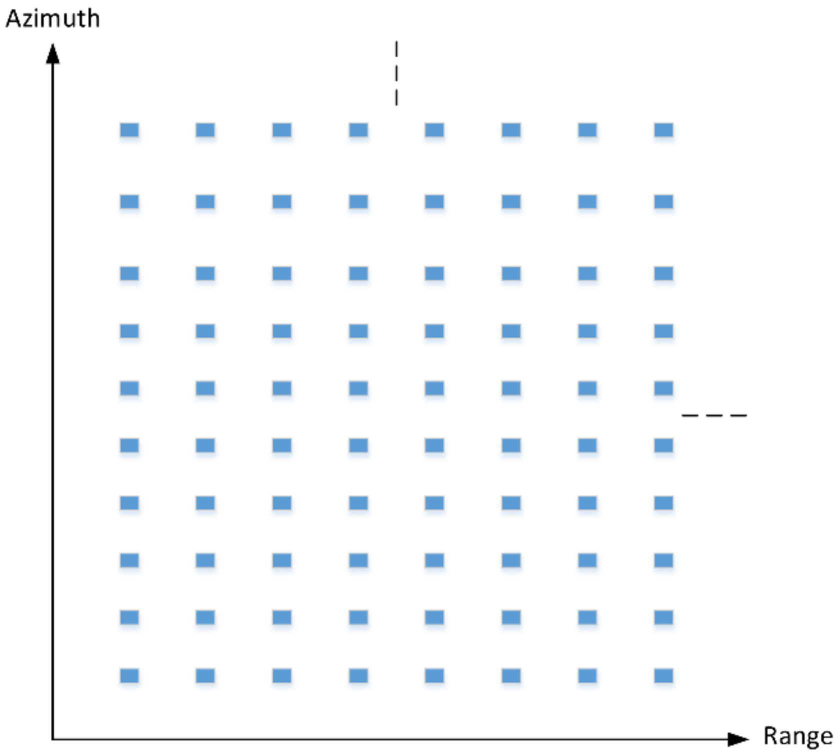

Figure 3.1 Conventional sampling of SAR data[43].

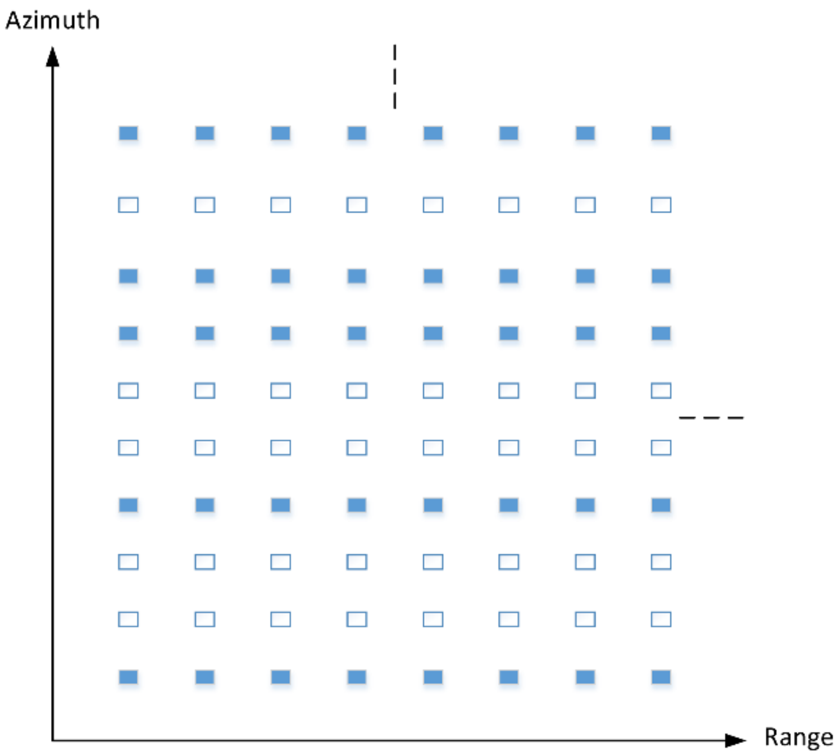

Figure 3.2 Slow-time undersampling of SAR data[43].

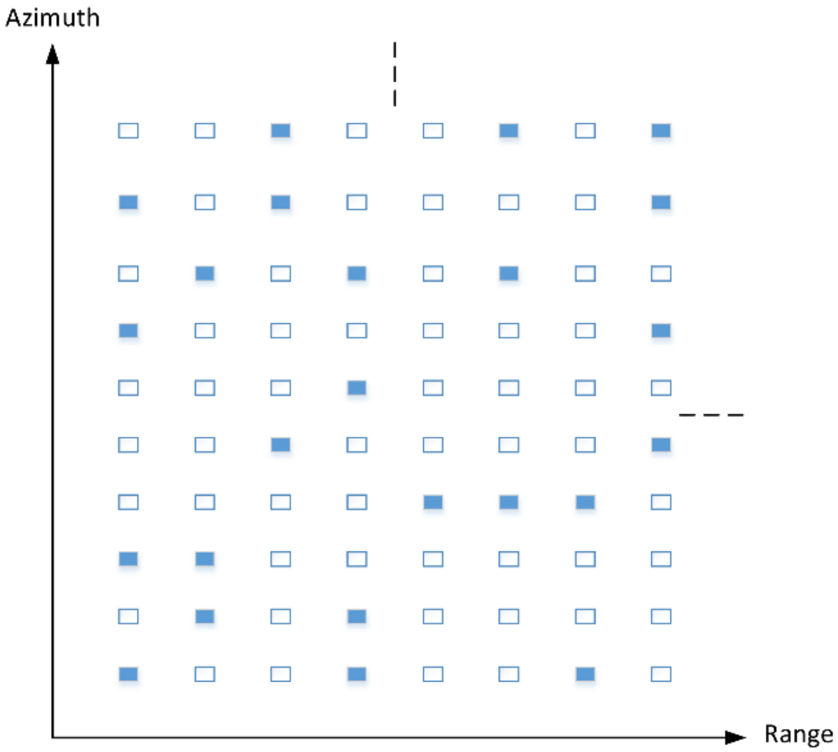

Figure 3.3 Random undersampling of SAR data in slow-time and fast-time[43].

3.2 1-Bit CS

CS facilitates the work of ADC by reducing the sampling rate. In addition, ADCs must also perform quantization. Normally, ADCs convert each measurement to a digital signal which has a specific bit depth in conventional CS framework. In the quantization process, the quantization error may increase depending on the bit depth. In the case of conventional CS algorithms, if the bit length is above a certain level, the quantization error is accepted within the normal measurement error and no special operation is performed for this error. However, when the measurements are quantized to digital signal with low bit length, this time the quantization error will increase and special algorithms should be developed for this quantization framework. In this thesis, we have developed the algorithm to obtain images from 1-bit quantized compressed SAR data, which is very extreme situation.

Quite a few algorithms have been proposed to reconstruct signal from 1-bit quantized measurements in CS literature. In fact, what is in 1-bit CS is recovering signal from the sign information of measurements. In 1-bit quantized data, the magnitude information of the signal is lost. In this case, it becomes impossible to reconstruct the signal exactly. In order to overcome this problem, two following methods have been used in 1-bit CS literature: In the first, unit-norm constraint is added to the optimization problem. In the second, normal or logistic distribution functions have been used to measure the consistency between reconstructed signal and 1-bit quantized measurement. In general, we can explain the 1-bit CS method as follows.

$$\mathbf{y} = sign(\mathbf{r}) = sign(\mathbf{A}\mathbf{x}) \tag{3.1}$$

(3.1) is sign measurement function and it is element-wise on the vector. The following optimization problem is tried to be solved in 1-bit CS.

$$\min_{\mathbf{x}} \|\mathbf{x}\|_1 \quad \text{subject to} \quad \mathbf{y} \odot \mathbf{A}\mathbf{x} \succeq \mathbf{0} \quad \text{and} \quad \|\mathbf{x}\|_2 = 1 \tag{3.2}$$

This optimization problem (3.2) is non-convex because unit-norm constraint $\|\mathbf{x}\|_2 = 1$ is imposed on it. In 1-bit CS mapping, an embedding property has been achieved similar to the RIP for real-valued measurements in CS. A distance metric is used for signal space in the Binary ϵ-Stable Embedding. The vector in distance metric measurement has the following benefit with unit-norm: when comparing two vectors, the magnitude of two vectors are identical and only the angle between them becomes important[21].

Another important method is to use logistic and normal distribution functions for consistency between the 1-bit quantized data and the recovered signal. In this solution method of 1-bit CS problem, unit-norm constraint is no longer required and the logarithm of consistency function is taken to convex the problem. This method can be roughly expressed as the following unconstrained optimization problem.

$$\arg\min_{\mathbf{x}} -\sum \log(\sigma(y_i \mathbf{x}^T \mathbf{a}_i)) + \tau \|\mathbf{x}\|_1 \tag{3.3}$$

where $\mathbf{a}_i$ is the ith row of the measurement matrix $\mathbf{A}$. σ is the consistency function where it can be logistic or normal distribution. y_i can be defined as the ith element of the sign vector $\mathbf{y}$.

3.3 1-Bit Quantization of SAR Data with Time-Varying Thresholds

In 1-bit CS setting, 1-bit quantized measurements give no information about the norm of the reconstructed signal, so classical 1-bit CS reconstruction methods assume $\|\mathbf{x}\|_2 = 1$. However, a recent study[30] showed that in 1-bit CS setting, the norm of the reconstructed signal, i.e., the magnitude of the reconstructed signal, can be recovered more precisely without the need for unit-norm constraint or the consistency function. This method allows the calculation of the signal norm by adding the affine shifts to the measurements which will be quantized to 1-bit. Under normal conditions, measurements are being quantized by comparing to a zero threshold in 1-bit CS setting. In the proposed method, measurements are quantized to 1-bit by comparing to time-varying thresholds.

Now we can explain how 1-bit quantization with time-varying thresholds is performed in spotlight-mode SAR imaging. The observation model of spotlight-mode SAR imaging (2.9) have been examined in Chapter 2. The mathematical model of spotlight SAR is as follows

$$r_\theta(t) = \mathbf{H}_\theta(t)\mathbf{f} + \epsilon(t) \tag{3.4}$$

Sign measurements of in-phase and quadrature channels are retained separately in 1-bit quantisation framework. The observed data are sampled at sampling times t_j at the ith viewing angle for real and imaginary parts separately before quantising to 1-bit with time-varying thresholds. The demodulated and sampled signal is then compared to time-varying threshold $h_i(t) = h_{R_i}(t) + jh_{I_i}(t) \in \mathbb{C}$ at each azimuth position and the sign of the resulting difference is evaluated separately for real and imaginary parts at angle θ_i. We consider h_{R_i} and h_{I_i} as independent and identically distributed (i.i.d) Gaussian random variables. In this work, we pick the standard deviation (σ) of $\mathbb{N}(0, \sigma^2)$ as ℓ_2-norm of the original underlying scene in the simulations to obtain simplified error estimate[30]. In practice, SAR images which are reconstructed by 1-bit MF can be used to find the ℓ_2-norm of the underlying scene before BCST-SAR is applied. Time-varying thresholds are drawn once and fixed thereafter. Defining $y_i = y_{R_i} + y_{I_i}$ denote the observed data which is quantised to 1-bit with time-varying thresholds at time t for each viewing angle θ_i.

$$
\begin{aligned}
y_{R_i}(t) =& sign(\Re[r_{\theta_i}(t)] - h_{R_i}(t)) \\
=& sign(\Re[\mathbf{H}_{\theta_i}\mathbf{f} + \epsilon_i(t)] - h_{R_i}(t))
\end{aligned} \tag{3.5}
$$

$$
\begin{aligned}
y_{I_i}(t) =& sign(\Im[r_{\theta_i}(t)] - h_{I_i}(t)) \\
=& sign(\Im[\mathbf{H}_{\theta_i}\mathbf{f} + \epsilon_i(t)] - h_{I_i}(t))
\end{aligned} \tag{3.6}
$$

in which $\Re[\cdot]$ and $\Im[\cdot]$ denote the real and imaginary parts, respectively[34, 35], θ_i, $i = 1, 2, \cdots, P$ are viewing angles and

$$
sign(x) = \begin{cases} +1, & x \geq 0 \\ -1, & x < 0 \end{cases} \tag{3.7}
$$

Let $\mathbf{y}_{R_i}$ and $\mathbf{y}_{I_i}$ be the column vectors of the samples which are quantised to 1-bit and can be expressed compactly as follows:

$$
\begin{cases} \mathbf{y}_R = [\mathbf{y}_{R_1}, \mathbf{y}_{R_2}, \cdots, \mathbf{y}_{R_P}]^T \\ \mathbf{y}_I = [\mathbf{y}_{I_1}, \mathbf{y}_{I_2}, \cdots, \mathbf{y}_{I_P}]^T \end{cases} \tag{3.8}
$$

where $[\cdot]^T$ denotes the transpose of a matrix. Threshold values can be defined in vector form as follows:

$$
\begin{cases} \mathbf{h}_R = [\mathbf{h}_{R_1}, \mathbf{h}_{R_2}, \cdots, \mathbf{h}_{R_P}]^T \\ \mathbf{h}_I = [\mathbf{h}_{I_1}, \mathbf{h}_{I_2}, \cdots, \mathbf{h}_{I_P}]^T \end{cases} \tag{3.9}
$$

$\mathbf{H}_{\theta_i}$ is the discretized approximation of the observation kernel at angle θ. We can stack all $\mathbf{H}_{\theta_i}$ into a vector in order to facilitate the representation of equation, and it can be stated as

$$
\mathbf{H} = [\mathbf{H}_{\theta_1}, \mathbf{H}_{\theta_2}, \cdots, \mathbf{H}_{\theta_P}]^T \tag{3.10}
$$

After random sampling, 1-bit CS-based SAR imaging becomes inversion of the reflectivity field $\mathbf{f} \in \mathbb{C}^N$ from the 1-bit quantised observed data $\mathbf{y}_R + j\mathbf{y}_I \in \mathbb{C}^M$ and complex-valued discrete SAR projection operator $\mathbf{H} \in \mathbb{C}^{M \times N}$. In order to ease the derivation, all aforementioned complex-valued vectors and matrices must be transformed into real-valued domain

$$\mathbf{y} = \begin{bmatrix} \mathbf{y}_R \\ \mathbf{y}_I \end{bmatrix}, \quad \mathbf{A} = \begin{bmatrix} \Re(\mathbf{H}) & -\Im(\mathbf{H}) \\ \Im(\mathbf{H}) & \Re(\mathbf{H}) \end{bmatrix}, \quad \mathbf{x} = \begin{bmatrix} \Re(\mathbf{f}) \\ \Im(\mathbf{H}) \end{bmatrix}, \quad \mathbf{n} = \begin{bmatrix} \Re(\epsilon) \\ \Im(\epsilon) \end{bmatrix}, \quad \mathbf{h} = \begin{bmatrix} \mathbf{h}_R \\ \mathbf{h}_I \end{bmatrix} \tag{3.11}$$

3.4 Problem Formulation

In this study, we formulate 1-bit CS SAR image reconstruction problem as an unconstrained optimisation problem. We then turn it into a constrained optimisation formulation using variable splitting[36]. Since the objective function to be minimised is composed of the sum of two functions in this problem, it is better to split the variable x into a pair of variables. Then, the sum of two functions is minimized under the constraint that two variables have to be equal to each other. The constrained optimisation problem is tackled using an Augmented Lagrangian (AL) scheme with norm-squared error term. The optimisation problem that arises after AL method is solved by ADMM[50]. ADMM divides this resulting function into simpler sub-problems and performs sequential updates that are easy to implement. ADMM is fast because these separated sub-problems have closed-form formulations. One step includes a quadratic cost and the other step involves a Moreau proximal mapping in our problem.

In 1-bit CS SAR imaging, our aim is to estimate complex-valued reflectivity field vector from 1-bit quantised measurements. The $\mathbf{y}$ vector consists only of the sign values. Considering a $\mathbf{b}$ vector that is equal to the magnitude of $(\mathbf{Ax} - \mathbf{h})$, the multiplication of $\mathbf{b}$ vector with the sign values yields approximately $(\mathbf{Ax} - \mathbf{h})$. We can express this by the following formula[33]

$$\mathbf{y} \odot \mathbf{b} = \mathbf{Ax} - \mathbf{h} \tag{3.12}$$

where $\odot$ is the Hadamard product of vectors and matrices. As a result, the 1-bit CS SAR imaging problem can be described as

$$\min_{\mathbf{x} \in \mathbb{R}^{2N}, \mathbf{b} \in \mathbb{R}^{2M}} \|\mathbf{Ax} - \mathbf{y} \odot \mathbf{b} - \mathbf{h}\|_2^2 + \tau\phi(\mathbf{x}) \tag{3.13}$$

$\|\cdot\|_2$ is the ℓ_2-norm and $\phi(\mathbf{x})$ is the regularization function which is often nonsmooth. $\tau \geq 0$ is the regularization parameter. The scene to be imaged is supposed to be sparse, as is true for most inverse SAR (ISAR) and some specific SAR applications which include strong scatterers in a weak background[51]. ℓ_1-norm is a widely used sparsity regularization function that enforces sparse solutions. Therefore, in our study, ℓ_1-norm of the reflectivity field vector $\mathbf{f}$ is selected as the regularisation function. We can write ℓ_1-norm of $\mathbf{f}$ in $\mathbf{x}$ as $\|\mathbf{f}\|_1 = \sum_{i=1}^{N} \sqrt{\mathbf{x}_i^2 + \mathbf{x}_{i+N}^2}$. When we combine the data-fidelity and sparsity regularization functions, the objective function becomes

$$\min_{\mathbf{x}\in\mathbb{R}^{2N},\mathbf{b}\in\mathbb{R}^{2M}} \|\mathbf{A}\mathbf{x} - \mathbf{y} \odot \mathbf{b} - \mathbf{h}\|_2^2 + \tau \sum_{i=1}^{N} \sqrt{\mathbf{x}_i^2 + \mathbf{x}_{i+N}^2} \tag{3.14}$$

There are many ways to solve problem (3.14). We use ADMM-based approach, which is successfully applied to many signal and image reconstruction problems.

3.5 One-Bit CS SAR Imaging by Variable Splitting and ADMM

3.5.1 Variable Splitting

The objective function (3.14) is the sum of two functions. When the variable is split into two variables, each of which is the argument of each of two functions, the sum of two functions can be minimized under the constraint that two variables must be equal to each other. We can write the obtained unconstrained optimization problem in the following form

$$\min_{\mathbf{x}\in\mathbb{R}^{2N}} f_1(\mathbf{x}) + f_2(g(\mathbf{x})) \tag{3.15}$$

Since the variable splitting is a method that facilitates the solution of unconstrained optimization problem, it has been previously used many signal/image processing problems[36, 52, 53]. After a new variable $\mathbf{v}$, which is the argument of f_2, is created, the problem (3.15) is under the constraint $g(\mathbf{x}) = \mathbf{v}$. In this case, the unconstrained optimization problem becomes

$$\min_{\mathbf{x}\in\mathbb{R}^{2N},\mathbf{v}\in\mathbb{R}^{2N}} f_1(\mathbf{x}) + f_2(\mathbf{v}) \quad \text{subject to} \quad g(\mathbf{x}) = \mathbf{v} \tag{3.16}$$

It is clear that problem (3.16) is directly equal to the unconstrained problem (3.15). If g is linear, $g(\mathbf{x}) = \mathbf{G}\mathbf{x}$. This variable splitting leads to the following constrained optimization problem

$$\min_{\mathbf{x}\in\mathbb{R}^{2N},\mathbf{v}\in\mathbb{R}^{2N}} f_1(\mathbf{x}) + f_2(\mathbf{v}) \quad \text{subject to} \quad \mathbf{Gx} = \mathbf{v} \tag{3.17}$$

The main idea behind variable splitting is that solving the constrained problem is easier than solving the unconstrained one. As illustrated in the following equation, the constrained problem (3.16) has been tried to be solved by using a quadratic penalty function in [52] and [53].

$$\min_{\mathbf{x}\in\mathbb{R}^{2N},\mathbf{v}\in\mathbb{R}^{2N}} f_1(\mathbf{x}) + f_2(\mathbf{v}) + \frac{\alpha}{2}\|g(\mathbf{x}) - \mathbf{v}\|_2^2 \tag{3.18}$$

In this method, the objective function is being minimized alternately with respect to $\mathbf{x}$ and $\mathbf{v}$. While solving this problem α becomes very large and this situation makes the optimization problem ill-conditioned. So ADMM uses AL instead of a quadratic penalty function in the solution.

3.5.2 ADMM Algorithm

Augmented Lagrangian Method

AL method also known as method of multipliers arises from the application of proximal algorithm to the dual problem of a constrained optimization problem[54]. In this way, the constrained optimization problem is broken into a sequence of easier unconstrained optimization problems that can be solved by fast and reliable algorithms like Newton, quasi-Newton and conjugate gradient. Now let's examine the following constrained optimization problem

$$\min_{\mathbf{w}\in\mathbb{R}^{2N}} D(\mathbf{w}) \quad \text{subject to} \quad \mathbf{Kw} - \mathbf{c} = \mathbf{0} \tag{3.19}$$

The AL function of this problem is given below

$$L(\mathbf{w},\lambda) = D(\mathbf{w}) + \lambda^T(\mathbf{c} - \mathbf{Kw}) + \frac{\mu}{2}\|\mathbf{Kw} - \mathbf{c}\|_2^2 \tag{3.20}$$

where λ is the Lagrange multipliers vector and μ is the penalty parameter. The AL method or method of multipliers is given in Table 3.1.

Table 3.1 Augmented Lagrangian Algorithm.

Algorithm1: Augmented Lagrangian Method
1. Set $k = 0$. Choose $\mu > 0$, and λ^o
2. **Repeat**
3. $\mathbf{w}^{k+1} \in \arg\min_{\mathbf{w}} L(\mathbf{w}, \lambda^k)$
4. $\lambda^{k+1} = \lambda^k + \mu(\mathbf{K}\mathbf{w}^{k+1} - \mathbf{c})$
5. $k \leftarrow k + 1$
6. **Until** some stopping criteria is satisfied.

Iteration number is given as a superscript in our study. In the AL method, there is no need for μ to go to infinity for the solution of the problem as in the quadratic penalty approach[36]. In the AL function, the expressions that are outside of $D(\mathbf{w})$ can be written as a single quadratic term. If the standard complete the square procedure is applied to the AL function, the following form of AL method appears.

Table 3.2 Alternative form of Augmented Lagrangian algorithm.

Algorithm2: Alternative form of Augmented Lagrangian method
1. Set $k = 0$. Choose $\mu > 0$ and $\mathbf{d}^o$
2. **Repeat**
3. $\mathbf{w}^{k+1} \in \arg\min_{\mathbf{w}} D(\mathbf{w}) + (\mu/2)\|\mathbf{K}\mathbf{w} - \mathbf{c}\|_2^2$
5. $\mathbf{d}^{k+1} = \mathbf{d}^k - \mathbf{K}\mathbf{w}^{k+1} + \mathbf{c}$
6. $k \leftarrow k + 1$
7. **Until** some stopping criteria is satisfied.

The AL method produces the same sequence as a proximal algorithm which is applied to the dual problem of constrained optimization problem (3.19). In this solution method, $\mathbf{d}^k$ vector approximates to the solution of the dual problem while $\mathbf{w}^k$ converging to the solution of the primal problem (3.19)[54].

Application of Augmented Lagrangian Method to Variable Splitted Problem

Now we can explain how AL method can be applied to the variable splitting problem. Reconsidering the problem (3.17) again.

$$\min_{\mathbf{x}\in\mathbb{R}^{2N},\mathbf{v}\in\mathbb{R}^{2N}} f_1(\mathbf{x}) + f_2(\mathbf{v}) \quad \text{subject to} \quad \mathbf{Gx} = \mathbf{v} \tag{3.21}$$

This problem can be written in the form of a constrained optimization problem in (3.19) as follows:

$$\mathbf{w} = \begin{bmatrix} \mathbf{x} \\ \mathbf{v} \end{bmatrix}, \quad \mathbf{c} = \mathbf{0}, \quad \mathbf{K} = [\mathbf{G} - \mathbf{I}] \quad \text{and} \quad D(\mathbf{w}) = f_1(\mathbf{x}) + f_2(\mathbf{v}) \tag{3.22}$$

These definitions are placed in step 3 and 4 of Algorithm2 and the following expressions appear

$$(\mathbf{x}^{k+1}, \mathbf{v}^{k+1}) \in \arg\min_{\mathbf{x},\mathbf{v}} f_1(\mathbf{x}) + f_2(\mathbf{v}) + \frac{\mu}{2}\|\mathbf{Gx} - \mathbf{v} - \mathbf{d}^k\|_2^2 \tag{3.23}$$

$$\mathbf{d}^{k+1} = \mathbf{d}^k - \mathbf{Gx}^{k+1} + \mathbf{v}^{k+1} \tag{3.24}$$

In this case, the constrained problem has been transformed into a number of unconstrained optimization problems that can be more easily solved. In problem (3.23), the minimization can be performed efficiently by alternately minimizing with respect to $\mathbf{x}$ and $\mathbf{v}$, separately. This separation of variables turns out that the resulting algorithm which is called as alternating direction method of multipliers (ADMM)[36, 37, 50, 55, 56]. ADMM algorithm is given as follows:

Table 3.3 Alternating Direction Method of Multipliers.

Algorithm3: ADMM
1. Set $k = 0$. Choose $\mu > 0$, $\mathbf{v}^{\mathrm{o}}$ and $\mathbf{d}^{\mathrm{o}}$
2. **Repeat**
3. $\mathbf{x}^{k+1} \in \arg\min_{\mathbf{x}} f_1(\mathbf{x}) + (\mu/2)\|\mathbf{G}\mathbf{x} - \mathbf{v}^k - \mathbf{d}^k\|_2^2$
4. $\mathbf{v}^{k+1} \in \arg\min_{\mathbf{v}} f_2(\mathbf{v}) + (\mu/2)\|\mathbf{G}\mathbf{x}^{k+1} - \mathbf{v} - \mathbf{d}^k\|_2^2$
5. $\mathbf{d}^{k+1} = \mathbf{d}^k - \mathbf{G}\mathbf{x}^{k+1} + \mathbf{v}^{k+1}$
6. $k \leftarrow k + 1$
7. **Until** some stopping criteria is satisfied.

Convergence of ADMM

Consider the following form of the constrained optimization problem (3.17) with $g(\mathbf{x}) = \mathbf{G}\mathbf{x}$

$$\min_{\mathbf{x}\in\mathbb{R}^{2N}} f_1(\mathbf{x}) + f_2(\mathbf{G}\mathbf{x}) \tag{3.25}$$

In [57], it has been shown that Douglas-Rachford splitting method is convergent if f_1 and f_2 functions are closed, proper, convex and $\mathbf{G}$ satisfies the full column rank requirement. That theory can be precisely expressed as: Let $\mu > 0$, $\mathbf{v}^{\mathrm{o}}$ and $\mathbf{d}^{\mathrm{o}}$ be the arbitrary values. Consider that $\eta_k \geq 0, \quad k = 0, 1, \ldots$ and $\nu_k \geq 0, \quad k = 0, 1, \ldots$ are two sequences. These sequences have the following property

$$\sum_{k=0}^{\infty} \eta_k < \infty \quad \text{and} \quad \sum_{k=0}^{\infty} \nu_k < \infty$$

Considering that $\mathbf{x}^k$, $\mathbf{v}^k$ and $\mathbf{d}^k$ sequences satisfy the following conditions

$$\eta_k \geq \|\mathbf{x}^{k+1} - \arg\min_{\mathbf{x}}\{f_1(\mathbf{x}) + (\mu/2)\|\mathbf{G}\mathbf{x} - \mathbf{v}^k - \mathbf{d}^k\|_2^2\}\|_2$$
$$\nu_k \geq \|\mathbf{v}^{k+1} - \{\arg\min_{\mathbf{v}}\{f_2(\mathbf{v}) + (\mu/2)\|\mathbf{G}\mathbf{x}^{k+1} - \mathbf{v} - \mathbf{d}^k\|_2^2\}\|_2$$
$$\mathbf{d}^{k+1} = \mathbf{d}^k - \mathbf{G}\mathbf{x}^{k+1} + \mathbf{v}^{k+1}$$

If the problem (3.17) has a solution, then the sequences $\mathbf{x}^k$, $\mathbf{v}^k$ and $\mathbf{d}^k$ converge. Otherwise, the sequences are divergent. As denoted in Table 3.3, the sequences meet the above defined conditions strictly ($\eta_k = 0$ and $\nu_k = 0$). In this case, the convergence of ADMM is guaranteed. ADMM and Douglas-Rachford splitting method is identical when they are applied to the dual problem of (3.17). For this reason, convergence theorem is proved in [57].

3.5.3 Application of ADMM to 1-Bit CS SAR

If variable splitting is applied to the problem (3.14), the following constrained optimization function is obtained

$$\min_{\mathbf{x}\in\mathbb{R}^{2N},\mathbf{b}\in\mathbb{R}^{2M},\mathbf{v}\in\mathbb{R}^{2N}} f_1(\mathbf{x}) + f_2(\mathbf{v}) \quad \text{subject to} \quad \mathbf{Gx} = \mathbf{v} \tag{3.26}$$

where

$$f_1(\mathbf{x}) = \|\mathbf{Ax} - \mathbf{y}\odot\mathbf{b} - \mathbf{h}\|_2^2, \quad f_2(\mathbf{v}) = \tau\sum_{i=1}^{N}\sqrt{\mathbf{v}_i^2 + \mathbf{v}_{i+N}^2} \quad \text{and} \quad \mathbf{G} = \mathbf{I} \tag{3.27}$$

The constrained optimisation problem that occurs as a result of variable splitting is handled by using AL scheme. The corresponding AL to problem (3.26) is

$$L = \|\mathbf{Ax} - \mathbf{y}\odot\mathbf{b} - \mathbf{h}\|_2^2 + \tau\sum_{i=1}^{N}\sqrt{\mathbf{v}_i^2 + \mathbf{v}_{i+N}^2} + \lambda^T(\mathbf{x} - \mathbf{v}) + \frac{\mu}{2}\|\mathbf{x} - \mathbf{v}\|_2^2 \tag{3.28}$$

where λ is a Lagrange multipliers vector. Linear and quadratic terms added to the objective function in AL can be written as a single quadratic term by means of completing the squares[36, 55, 50, 37, 56]

$$L = \|\mathbf{Ax} - \mathbf{y}\odot\mathbf{b} - \mathbf{h}\|_2^2 + \tau\sum_{i=1}^{N}\sqrt{\mathbf{v}_i^2 + \mathbf{v}_{i+N}^2} + \frac{\mu}{2}\|\mathbf{x} - \mathbf{v} - \mathbf{d}\|_2^2 \tag{3.29}$$

where $\mathbf{d}$ is a scaled dual variable. In this case, ADMM for the problem (3.26) consists of the following iterations:

$$\mathbf{x}^{k+1} = \arg\min_{\mathbf{x}\in\mathbb{R}^{2N}} \|\mathbf{Ax} - \mathbf{y}\odot\mathbf{b} - \mathbf{h}\|_2^2 + \frac{\mu}{2}\|\mathbf{x} - \mathbf{v}^k - \mathbf{d}^k\|_2^2 \tag{3.30}$$

$$\mathbf{b}^{k+1} = |\mathbf{A}\mathbf{x}^{k+1} - \mathbf{h}| \tag{3.31}$$

$$\mathbf{v}^{k+1} = \arg\min_{\mathbf{v}\in\mathbb{R}^{2N}} \tau \sum_{i=1}^{N} \sqrt{\mathbf{v}_i^2 + \mathbf{v}_{i+N}^2} + \frac{\mu}{2}\|\mathbf{x}^{k+1} - \mathbf{v} - \mathbf{d}^k\|_2^2 \tag{3.32}$$

$$\mathbf{d}^{k+1} = \mathbf{d}^k - \mathbf{x}^{k+1} + \mathbf{v}^{k+1} \tag{3.33}$$

Each step of this alternating minimization is simpler than minimizing the original unconstrained problem (3.14). (3.30) has a simple least squares solution and (3.32) can be recognized as the Moreau proximal mapping of $\sum_{i=1}^{N} \sqrt{\mathbf{v}_i^2 + \mathbf{v}_{i+N}^2}$. The Moreau proximal mapping of the regularization function can be computed efficiently as defined in (27) and (28). When $\mathbf{x}$ is minimized, $\mathbf{b}$ is also minimized due to the fact that $\mathbf{b}$ is directly dependent upon $\mathbf{x}$. For the convergence of ADMM, $\mathbf{G}$ needs to meet the full column rank condition. In our problem, this condition is satisfied because $\mathbf{G} = \mathbf{I}$. If problem (3.30) and (3.31) are solved exactly, then the convergence of the ADMM-based algorithm is guaranteed[36, 57].

After least squares solution of problem (3.30), the $\mathbf{x}$-update formulation can be written as follows:

$$\mathbf{x}^{k+1} = (\mathbf{A}^H\mathbf{A} + \mu\mathbf{I}_{2N})^{-1}[\mathbf{A}^H(\mathbf{y} \odot \mathbf{b}^k + \mathbf{h}) + \mu\mathbf{p}^k] \tag{3.34}$$

where $\mathbf{p}^k = \mathbf{v}^k + \mathbf{d}^k$ and $\mathbf{I}_{2N}$ is the $2N \times 2N$ identity matrix. How (3.34) is derived from (3.30) is given in detail in Appendix A. If Woodbury matrix inversion formula is applied to $(\mathbf{A}^H\mathbf{A} + \mu\mathbf{I}_{2N})^{-1}$ to reduce computational cost, $\mathbf{x}^{k+1}$ becomes

$$\mathbf{x}^{k+1} = \frac{1}{\mu}(\mathbf{I}_{2N} - \mathbf{A}^H(\mathbf{A}^H\mathbf{A} + \mu\mathbf{I}_{2M})^{-1}\mathbf{A})[\mathbf{A}^H(\mathbf{y} \odot \mathbf{b}^k + \mathbf{h}) + \mu\mathbf{p}^k] \tag{3.35}$$

The Moreau proximal mapping of $\frac{\tau}{\mu}\sum_{i=1}^{N} \sqrt{\mathbf{v}_i^2 + \mathbf{v}_{i+N}^2}$ in problem (3.32) can be defined as

$$\Psi_{\tau\phi/\mu}(\mathbf{z}) = \arg\min_{\mathbf{v}\in\mathbb{R}^{2N}} \{\frac{\tau}{\mu} \sum_{i=1}^{N} \sqrt{\mathbf{v}_i^2 + \mathbf{v}_{i+N}^2} + \frac{1}{2}\|\mathbf{v} - \mathbf{z}\|_2^2\} \tag{3.36}$$

where $\mathbf{z} = \mathbf{x}^{k+1} - \mathbf{d}^k$. The minimization with respect to $\mathbf{v}$ in problem (3.36) can be defined as N scalar convex minimizations by decoupling $\mathbf{v}$ into two-variable for $i = 1, 2, \ldots, N$[13]

$$\begin{pmatrix} \Psi_{\tau\phi/\mu}(\mathbf{z}_i) \\ \Psi_{\tau\phi/\mu}(\mathbf{z}_{i+\mathbf{N}}) \end{pmatrix} = \arg\min_{\zeta,\xi\in\mathbb{R}} \{ \frac{\tau}{\mu}\sqrt{\zeta^2+\xi^2} + \frac{1}{2}(\zeta-\mathbf{z}_i)^2 + \frac{1}{2}(\xi-\mathbf{z}_i)^2 \} \tag{3.37}$$

The minimization problem (3.37) has the following closed-form solutions[13]

$$\Psi_{\tau\phi/\mu}(\mathbf{z}_i) = (\sqrt{\mathbf{z}_i^2+\mathbf{z}_{i+N}^2} - \frac{\tau}{\mu})_+ \frac{\mathbf{z}_i}{\sqrt{\mathbf{z}_i^2+\mathbf{z}_{i+N}^2}} \tag{3.38}$$

$$\Psi_{\tau\phi/\mu}(\mathbf{z}_{i+\mathbf{N}}) = (\sqrt{\mathbf{z}_i^2+\mathbf{z}_{i+N}^2} - \frac{\tau}{\mu})_+ \frac{\mathbf{z}_{i+\mathbf{N}}}{\sqrt{\mathbf{z}_i^2+\mathbf{z}_{i+N}^2}} \tag{3.39}$$

for $i = 1, 2, \dots, N$ and where $(\omega)_+ = \max(\omega, 0)$. If all aforementioned formulations are combined, the ADMM-based algorithm for 1-bit CS SAR imaging is summarized as in the following Table 3.4

Table 3.4 BCST-SAR Algorithm.

Algorithm: BCST-SAR Algorithm for One-Bit CS SAR Imaging
1. Input $\mathbf{h} \in \mathbb{R}^{2M}$. Choose $\mu, \tau > 0, \mathbf{b}^0 \in \mathbb{R}^{2M}, \mathbf{v}^0 \in \mathbb{R}^{2N}, \mathbf{d}^0 \in \mathbb{R}^{2N}$
2. Set $k = 0, \mathbf{B} = (\mathbf{A}\mathbf{A}^H + \mu\mathbf{I}_{2M})^{-1}$
3. **Repeat**
4. $\mathbf{q}^k = \mathbf{A}^H(\mathbf{y} \odot \mathbf{b}^k + \mathbf{h}) + \mu(\mathbf{v}^k + \mathbf{d}^k)$
5. $\mathbf{x}^{k+1} = \frac{1}{\mu}\mathbf{q}^k - \frac{1}{\mu}\mathbf{A}^H\mathbf{B}\mathbf{A}\mathbf{q}^k$
6. $\mathbf{b}^{k+1} = \lvert\mathbf{A}\mathbf{x}^{k+1} - \mathbf{h}\rvert$
7. $\mathbf{v}^{k+1} = \mathbf{\Psi}_{\tau\phi/\mu}(\mathbf{x}^{k+1} - \mathbf{d}^k)$
8. $\mathbf{d}^{k+1} = \mathbf{d}^k - \mathbf{x}^{k+1} + \mathbf{v}^{k+1}$
9. $k \leftarrow k + 1$
10. **Until** some stopping criteria is satisfied.

We consider $\mathbf{h}_R$ and $\mathbf{h}_I$ as independent vectors of i.i.d. random variables with Gaussian distribution. They are drawn once and fixed thereafter while the measurements, which are taken from in-phase and quadrature channels of SAR system, are being quantized to 1-bit. Threshold vector $\mathbf{h}$ is known and used without being changed in the algorithm. It is given as an input to the BCST-SAR algorithm. $\mathbf{b}$ is initialized with $\mathbf{1}_{2M}$ vector. $\mathbf{d}$ and $\mathbf{v}$ vectors are initialized with $\mathbf{0}_{2N}$ vectors.

Computational Complexity of BCST-SAR Algorithm

In the proposed BCST-SAR algorithm, intensive computations occur in steps **S4** and **S5**. We set $\mathbf{B} = (\mathbf{A}\mathbf{A}^H + \mu\mathbf{I}_{2M})^{-1}$ prior to iteration. Cholesky factorization method is used to find the inverse of $\mathbf{A}\mathbf{A}^H + \mu\mathbf{I}_{2M}$ since the term is positive definite and factorization is done once before iteration starts. The cost for Cholesky factorisation in the algorithm is $\frac{8}{3}M^3$ flops. In step **S4**, the main computational complexity comes from the multiplication of $\mathbf{A}^H$ with $(\mathbf{y} \odot \mathbf{b}^k + \mathbf{h})$ and the cost is $8MN$ flops. Forward and backward substitutions are utilized in step **S5** and leading computational complexities arise from these substitutions. The cost of forward and backward substitutions is $8M^2$ flops.

When the algorithm converges, we find the estimation of $\mathbf{x}$, which is denoted by $\hat{\mathbf{x}}$. Then, the estimated $\hat{\mathbf{x}}$ vector is transformed into a complex-domain and the absolute value is taken to form the SAR image.

CHAPTER 4

SIMULATIONS

In this section, we carry out experiments to see whether the method we recommend for 1-bit CS SAR imaging works or not. We perform experiments using synthetic and real SAR images. Results will be compared with conventional 1-bit MF method and state-of-the-art BIHT[21] and MAP[13] algorithms that work well for 1-bit CS. There are two versions of BIHT algorithm, the standard BIHT (one-sided ℓ_1 objective) and BIHT-ℓ_2 (one-sided ℓ_2 objective). We used BIHT-ℓ_2 in our simulations since it gives better results in noisy cases. For the implementation, we utilized the BIHT demo[58]. Gaussian noise is added to the signal in each experiment. We have used the system parameters shown in the following Table 4.1 to generate the synthetic SAR phase history data. We have written the code of MAP algorithm[13] ourselves and given it in the Appendix C.

Table 4.1 SAR system parameters.

Parameters	Values
Carrier frequency	$1 \times 10^9 Hz$
Bandwidth	$200 \times 10^6 Hz$
Chirp rate	$200\pi \times 10^{12} rad/s^2$
Pulse duration	$10^{-6} s$
Synthetic aperture	$500m$

4.1 Points Targets Simulations

In the first experiment, five point targets placed randomly in the imaging scene are generated. All targets have uniform amplitude. The imaging scene has 200 m width in both azimuth and range directions. The space between each discretized scene points is 5 m. The performances of four algorithms are evaluated under two different SNR levels. The results are shown in Figures 4.1 and 4.2. Ghost targets that severely interfere with the target detection appear in 1-bit MF method at $SNR = 20\ dB$. Ghost targets disappear when $SNR = -20\ dB$ but this time, the noise floor increases and the quality of SAR image itself deteriorates. As can be seen in Figures 4.1 and 4.2, BIHT-ℓ_2, MAP and BCST-SAR algorithms outperform the conventional MF based method at both SNR values.

In this simulation, we choose $\tau = 5$, $\mu = 1$ for BCST-SAR and the sparsity constant K required for BIHT-ℓ_2 is selected as 5 because the cardinality of the support set of the sparse scene is 5. Three state-of-the-art algorithms alleviate the side-lobes and remove the ghost targets with 1-bit quantised data. It is enough to evaluate the log-intensity SAR images qualitatively for the first experiment. Our aim is to show that BCST-SAR eliminates ghost targets and generates SAR images with high resolution.

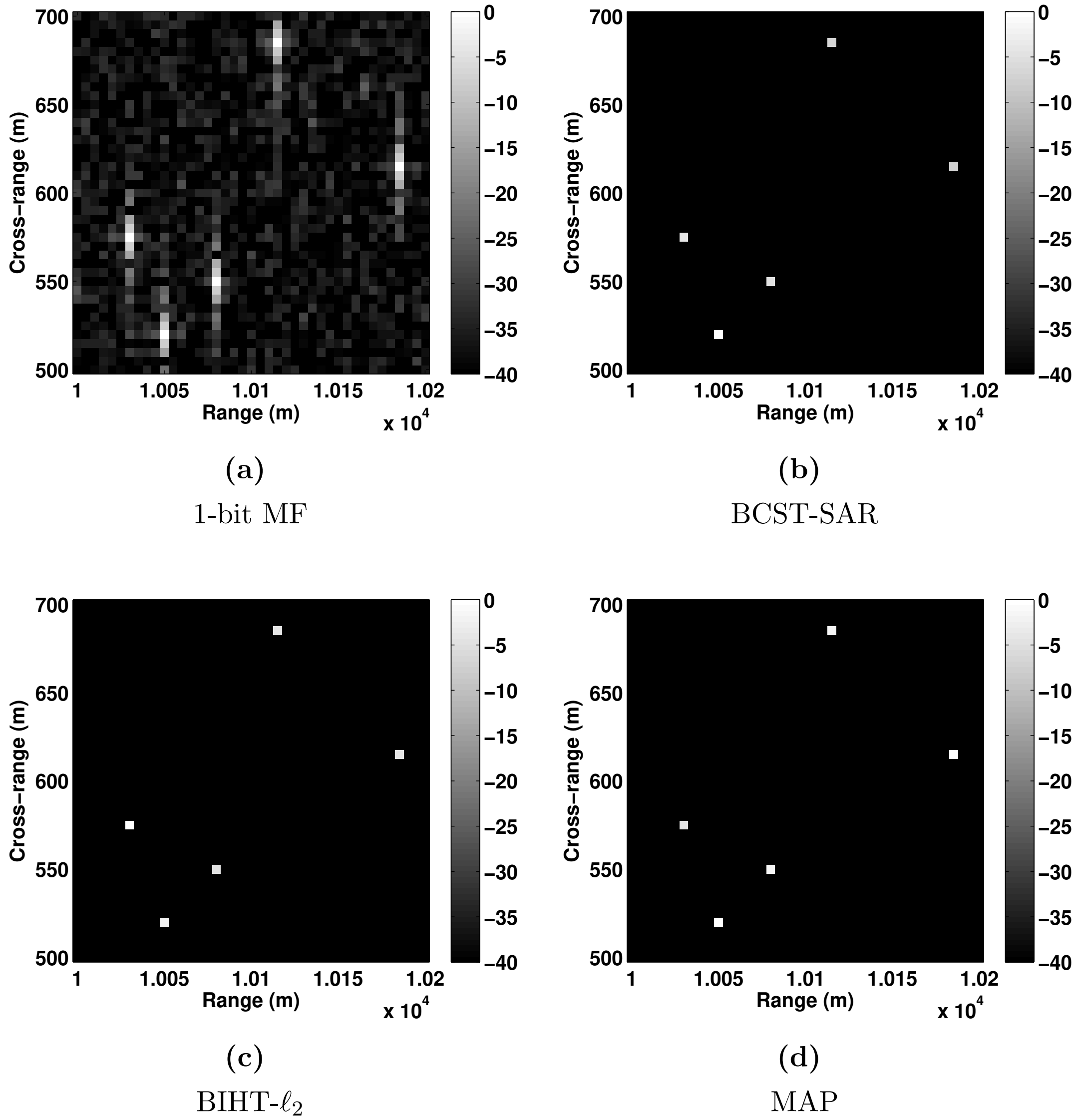

(a) 1-bit MF

(b) BCST-SAR

(c) BIHT-ℓ_2

(d) MAP

Figure 4.1 Reconstructed log-intensity images of randomly placed five point targets under $SNR = -20\ dB$.

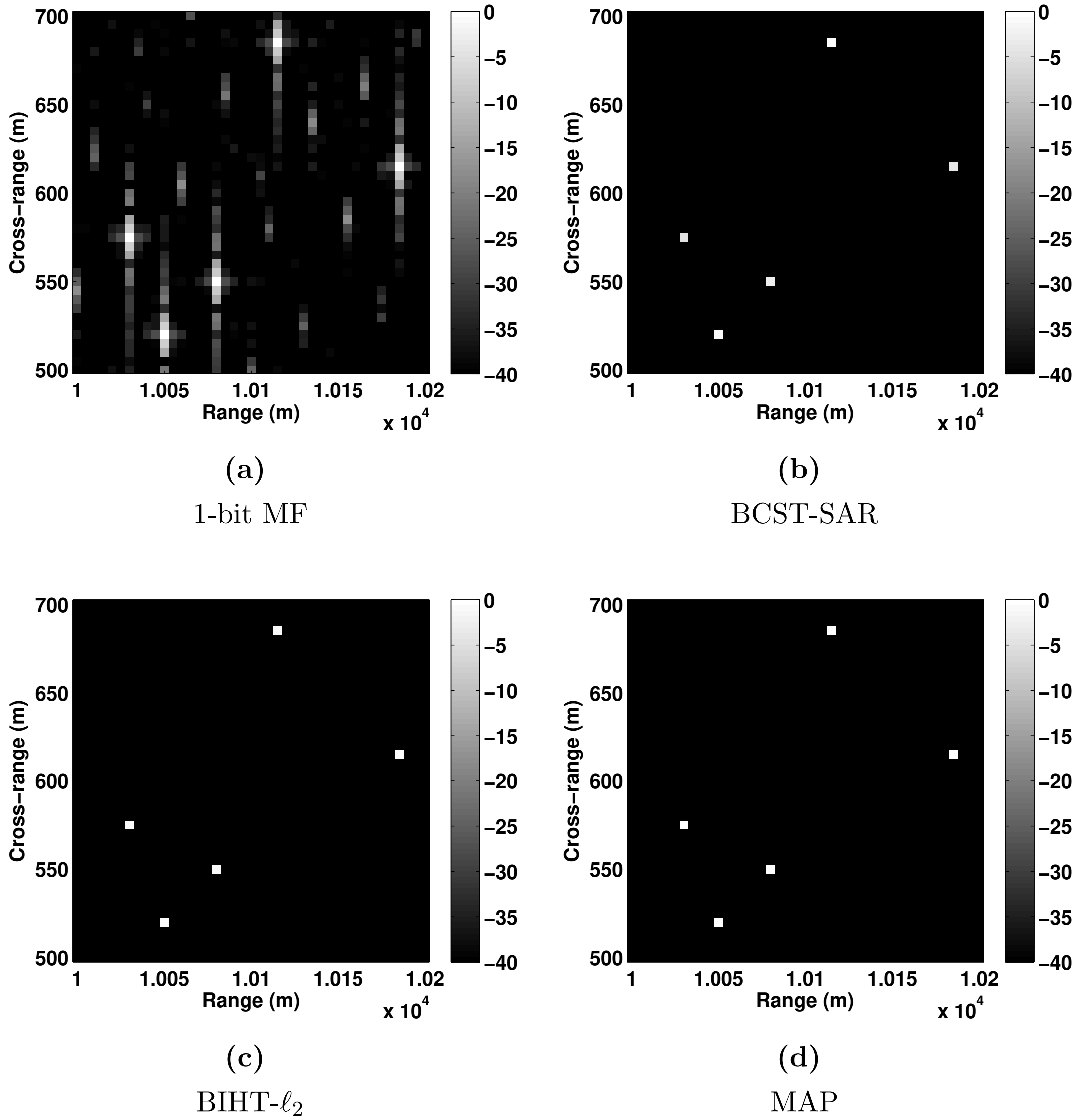

(a) 1-bit MF

(b) BCST-SAR

(c) BIHT-ℓ_2

(d) MAP

Figure 4.2 Reconstructed log-intensity images of randomly placed five point targets under $SNR = 20\ dB$.

4.2 Scene Sparsity versus pSNR for State-of-the-art Algorithms

Next, we evaluate the performances of BIHT-ℓ_2, MAP and proposed BCST-SAR algorithms for different sparsity levels using synthetically produced SAR data. The scene used for this evaluation is composed of point and rectangular-shaped targets. The sparsity level is increased from 5 to 50 and peak-Signal-to-Noise Ratio ($pSNR$) of the reconstructed images is used for the performance measurement. Scene sparsity level can be defined as the number of non-zero reflectivities in SAR image.

The reconstructions are performed for input SNR level of 20 dB. The parameter selection is made as $\tau = 20$ and $\mu = 1$ for BCST-SAR. For BIHT-ℓ_2, sparsity constant K is chosen as 20. The regularisation parameter λ is taken as 15 for MAP algorithm and 3.96% of full data have been used for three algorithms in this simulation. Sparsity levels versus $pSNR$ graph for three algorithms are illustrated in Figure 4.3. We observe from Figure 4.3 that $pSNR$ decreases as the sparsity level increased for BCST-SAR. $pSNR$ values of MAP algorithm are almost constant for sparsity level less than 25 but appear to decrease when sparsity level exceeds 25.

As can be seen from Figure 4.3, the proposed BCST-SAR approach outperforms MAP and BIHT-ℓ_2 methods at all sparsity levels. The reason behind the better performance of BCST-SAR is that the amplitude of the recovered SAR reflectivity by BCST-SAR is more exact since the time-varying thresholds are used in BCST-SAR method. As stated in [30], norm recovery is possible from 1-bit measurements which are formed using time-varying thresholds. However, in other methods, the amplitude information of the signal is lost by 1-bit quantization and it is impossible to recover the norm from these 1-bit measurements.

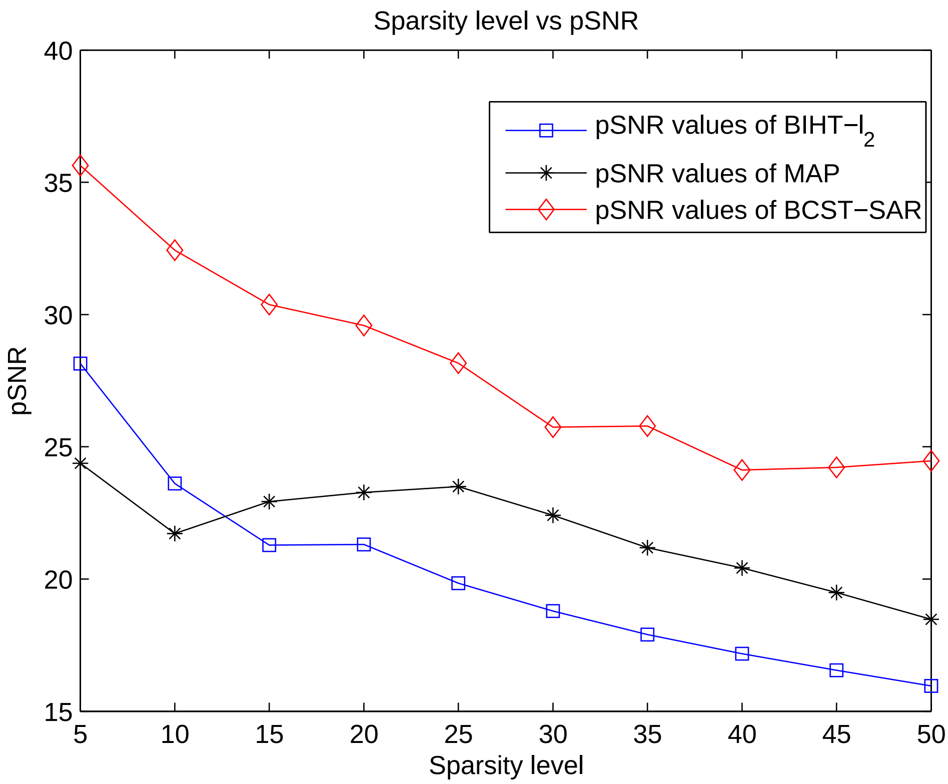

Figure 4.3 Scene sparsity versus $pSNR$ values of three algorithms under $SNR = 20\ dB$.

4.3 Particular Geometry Scene Simulations

In the next experiment, in order to assess the performances of the compared four methods, a synthetically produced radar scene with a certain geometric shape is utilized. The conventional 1-bit MF reconstruction is shown in Figure 4.4b. For this experiment, we set $\tau = 30$ and $\mu = 1$ in BCST-SAR. The sparsity constant K for BIHT-ℓ_2 is chosen as 55. Figures 4.4c, 4.4d and 4.4e demonstrate the reconstructed images obtained by BIHT-ℓ_2, MAP and BCST-SAR methods from only 3.96% of full aperture data. It should be noted that these three algorithms give good results for this experiment as well. Although the three algorithms give good results visually, the SAR image generated by the BCST-SAR algorithm is more precise.

To make a quantitative comparison of the performances of BIHT-ℓ_2, MAP and BCST-SAR algorithms, two quality metrics are used. These metrics are Mean-Square-Error (MSE) and Target-to-Background Ratio (TBR) which are defined as follows:

$$MSE = \frac{1}{I} \| |\mathbf{f}| - |\hat{\mathbf{f}}| \|_2^2 \tag{4.1}$$

$\mathbf{f}$ and $\hat{\mathbf{f}}$ denote the original and the reconstructed images, respectively. I is the total number of pixels in the SAR image.

Target-to-background ratio (TBR) is utilized to emphasize the target pixels with respect to the background:

$$TBR = 20 \log_{10}\left(\frac{max_{i \in T} |\hat{\mathbf{f}}_i|}{\frac{1}{N_B} \sum_{j \in B} |\hat{\mathbf{f}}_j|}\right) \tag{4.2}$$

T and B represent the pixel indices for the target and background regions, respectively. N_B is the total number of background pixels.

While comparing three methods, it is expected to lead lower MSE and higher TBR values for better reconstructions.

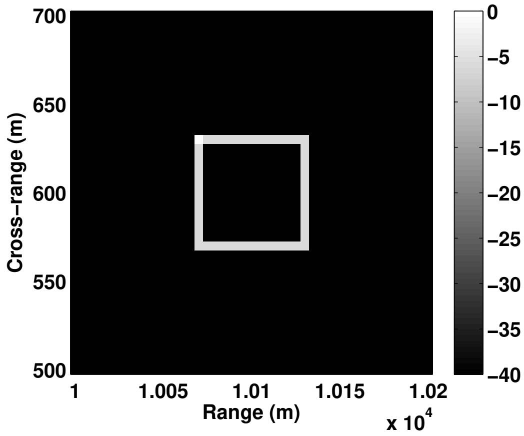

(a)
Original scene

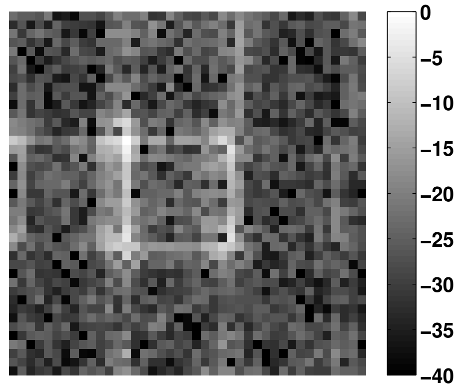

(b)
1-bit MF

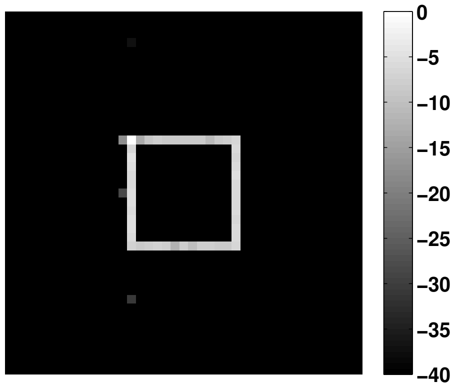

(c)
BIHT-ℓ_2

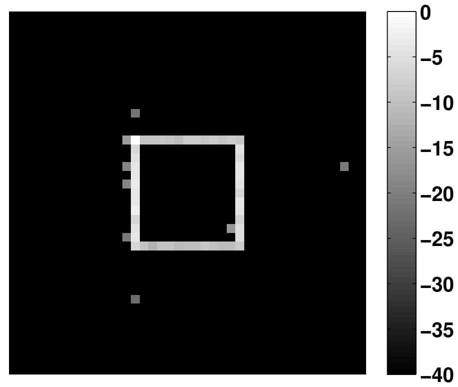

(d)
MAP

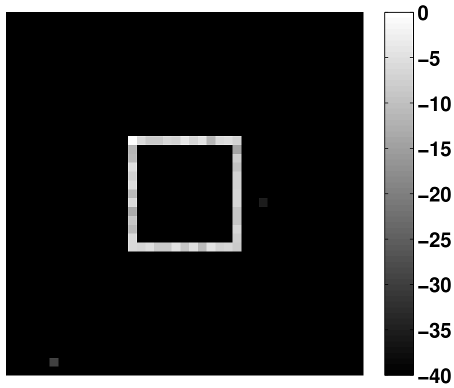

(e)
BCST-SAR

Figure 4.4 Reconstructed log-intensity images of particular geometry scene under $SNR = 20\ dB$.

Now we can present quantitative results for the experiments using these two metrics. Comparison results of BIHT-ℓ_2, MAP and BCST-SAR algorithms in terms of MSE and TBR for various SNR levels are demonstrated in Figures 4.5 and 4.6. While BIHT-ℓ_2, MAP and BCST-SAR are being implemented, 3.96% of full data have been used. The results in Figure 4.5 show that BCST-SAR provides much lower MSE values than BIHT-ℓ_2 and MAP methods. In Figure 4.6, BCST-SAR has a higher TBR value than BIHT-ℓ_2 and MAP algorithms. The performance of BCST-SAR is better than other algorithms in terms of MSE and TBR values because the norm value of the reconstructed SAR signal obtained by BCST-SAR is more accurate.

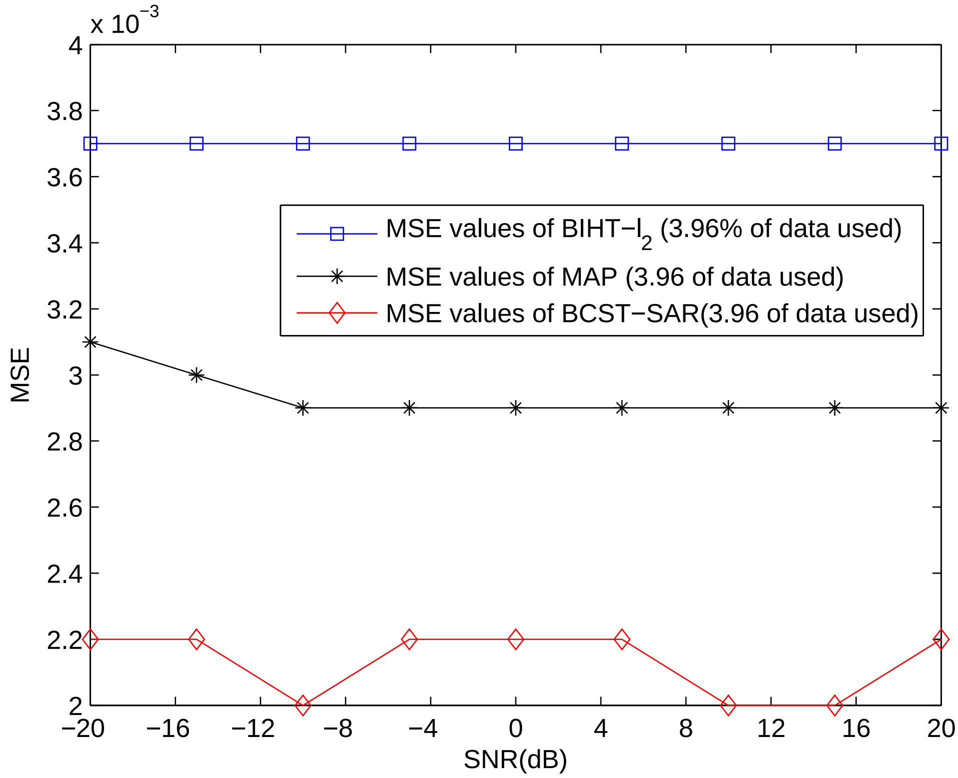

Figure 4.5 MSE values of the particular geometry scene experiment using BIHT-ℓ_2, MAP and BCST-SAR under different SNR levels.

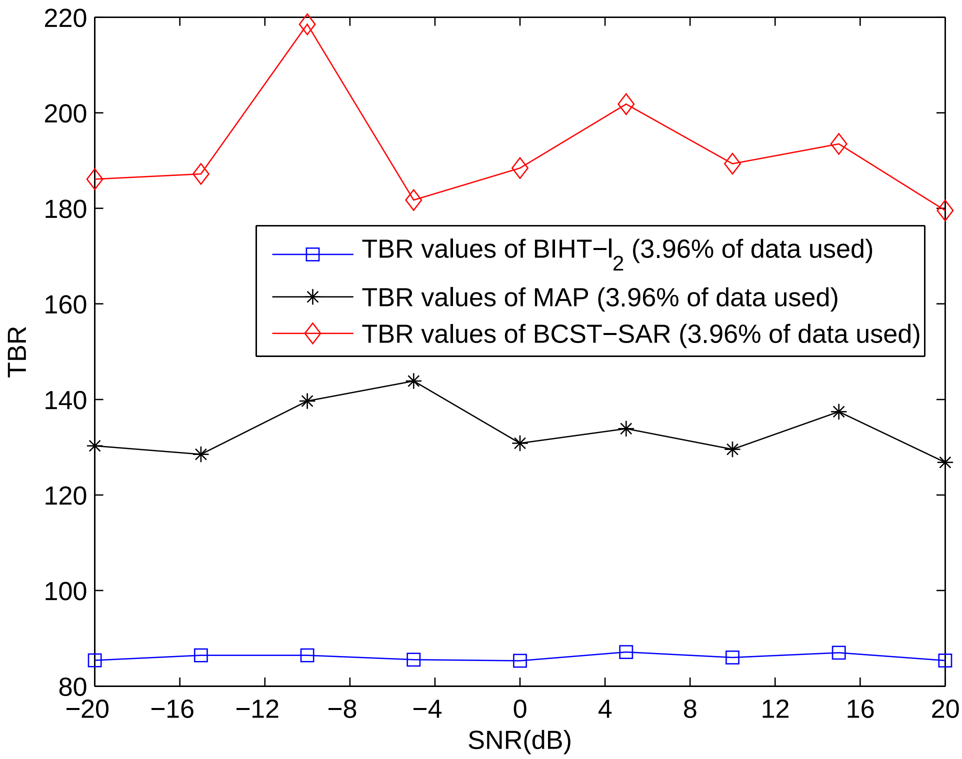

Figure 4.6 TBR values of the particular geometry scene experiment using BIHT-ℓ_2, MAP and BCST-SAR under different SNR levels.

BCST-SAR, MAP and BIHT-ℓ_2 are also compared for different measurement percentages. The results for this comparison are given in Table 4.2. BCST-SAR for all measurement percentages except 0.82% yields better MSE and TBR values than BIHT-ℓ_2 and MAP.

Table 4.2 Performance metrics for the particular geometry scene imagery reconstructed by BIHT-ℓ_2, MAP and BCST-SAR at different levels of measurement percentages ($SNR = 20\ dB$).

Measurement Percentage		MSE	TBR
0.82%	BIHT-ℓ_2	0.0039	108.3081
	MAP	0.0037	145.5284
	BCST-SAR	0.0039	103.1095
3.96%	BIHT-ℓ_2	0.0037	168.6127
	MAP	0.0028	145.0663
	BCST-SAR	0.0022	171.9432
4.90%	BIHT-ℓ_2	0.0037	183.2439
	MAP	0.0028	191.9402
	BCST-SAR	0.0019	201.3546
6.60%	BIHT-ℓ_2	0.0037	178.0042
	MAP	0.0027	153.6716
	BCST-SAR	0.0016	220.3040

4.4 SIR-C/X-SAR Image Simulations

In the last experiment, in order to further test the effectiveness of BCST-SAR, four reconstruction algorithms have been applied to a small part of data extracted from a real SIR-C/X-SAR image[2, 59]. The sparse part of the SAR image has been selected. SAR phase history have been generated by using the acquisition model expressed in [60] from the complex SAR image. The experiment is implemented under $SNR = 20\ dB$. Figure 4.7 shows the SAR images reconstructed by five different methods. Figure 4.7a shows the original underlying scene which is reconstructed by MF without quantization. Figure 4.7b demonstrates the MF reconstruction of SAR image with 1-bit quantized data. We can distinguish clearly high side-lobes in MF reconstructed images. We choose the regularization parameter $\tau = 130$ and $\mu = 1$ in BCST-SAR algorithm. Sparsity constant K required for BIHT-ℓ_2 is selected as 270. λ value of MAP algorithm for this simulation is chosen as 15.5

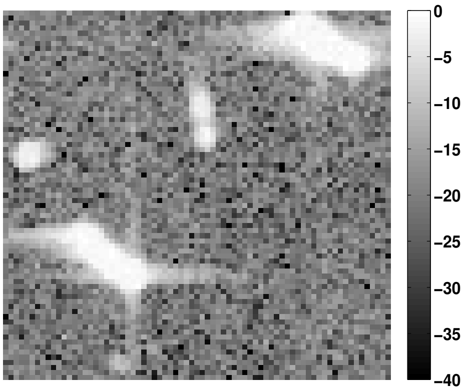

(a)
Conventional MF

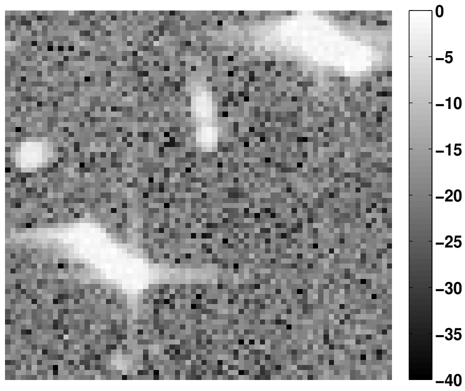

(b)
1-bit MF

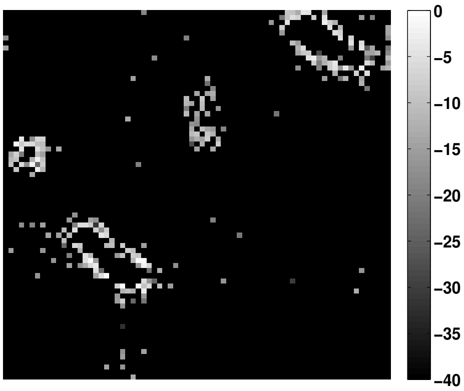

(c)
BIHT-ℓ_2

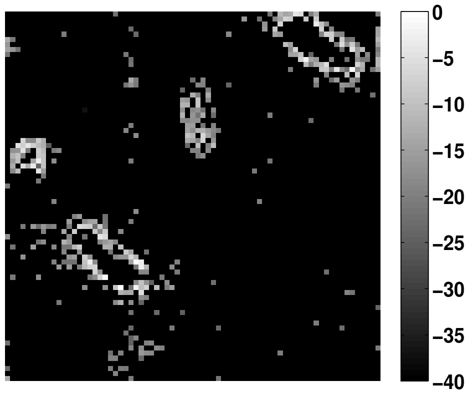

(d)
MAP

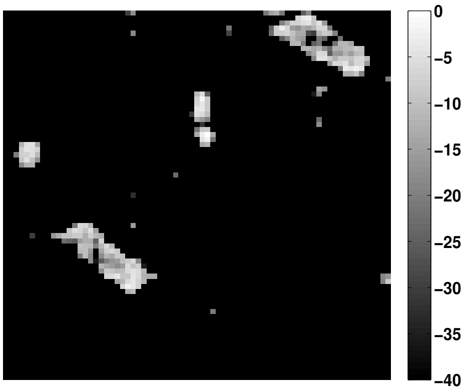

(e)
BCST-SAR

Figure 4.7 Reconstructed log-intensity images of a SAR data extracted from a real SIR-C/X-SAR image under $SNR = 20\ dB$.

It is not difficult to determine the sparsity constant K needed for BIHT-ℓ_2 in the previous experiments since the scene is produced synthetically. However, in the last experiment, we have decided the sparsity constant K after so many trials. Figures 4.7c,4.7d,4.7e illustrate the reconstructed images obtained by BIHT-ℓ_2, MAP and BCST-SAR from only 22.8% of full aperture data. As can be seen in Figures 4.7c,4.7d,4.7e, the images obtained by BIHT-ℓ_2, MAP and BCST-SAR have higher resolution and lower side-lobes. BCST-SAR achieves better reconstructions than all compared algorithms. Quantitative comparisons of BIHT-ℓ_2, MAP and BCST-SAR are also given for the last experiment. MSE and TBR values of the reconstructed images versus different $SNRs$ are presented in Figures 4.8 and 4.9. BCST-SAR produces lower MSE values than BIHT-ℓ_2 and MAP as shown in Figure 4.8. The image reconstructed by BCST-SAR has higher TBR values than the image obtained by BIHT-ℓ_2, and MAP as illustrated in Figure 4.9.

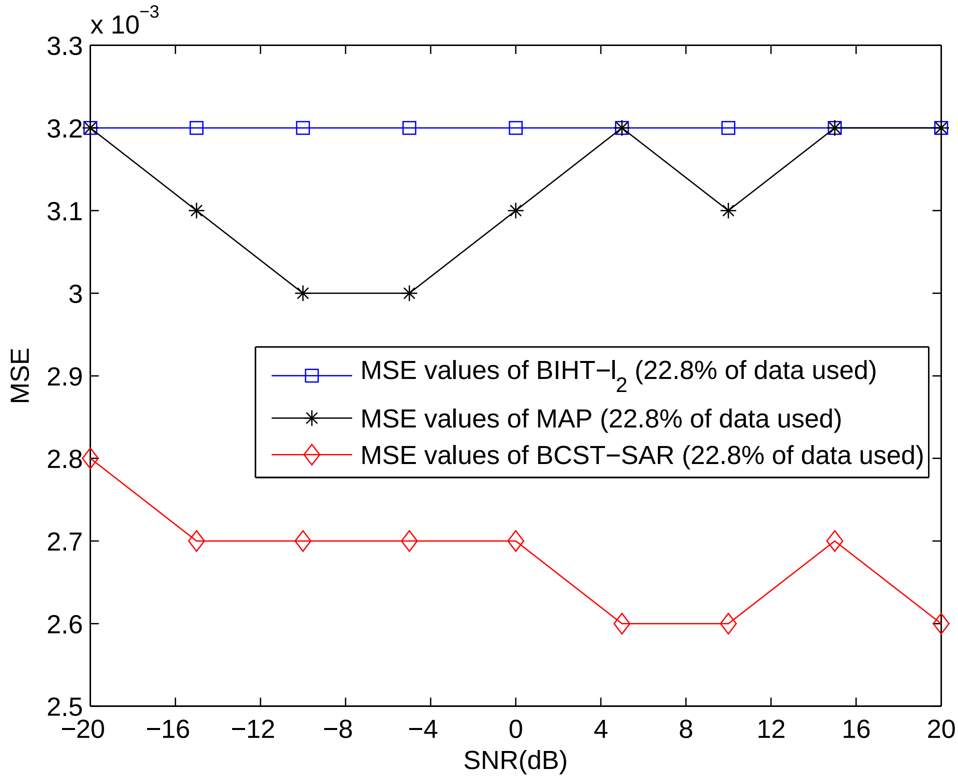

Figure 4.8 MSE values of the SIR-C/X-SAR image experiment using BIHT-ℓ_2, MAP and BCST-SAR under different SNR levels.

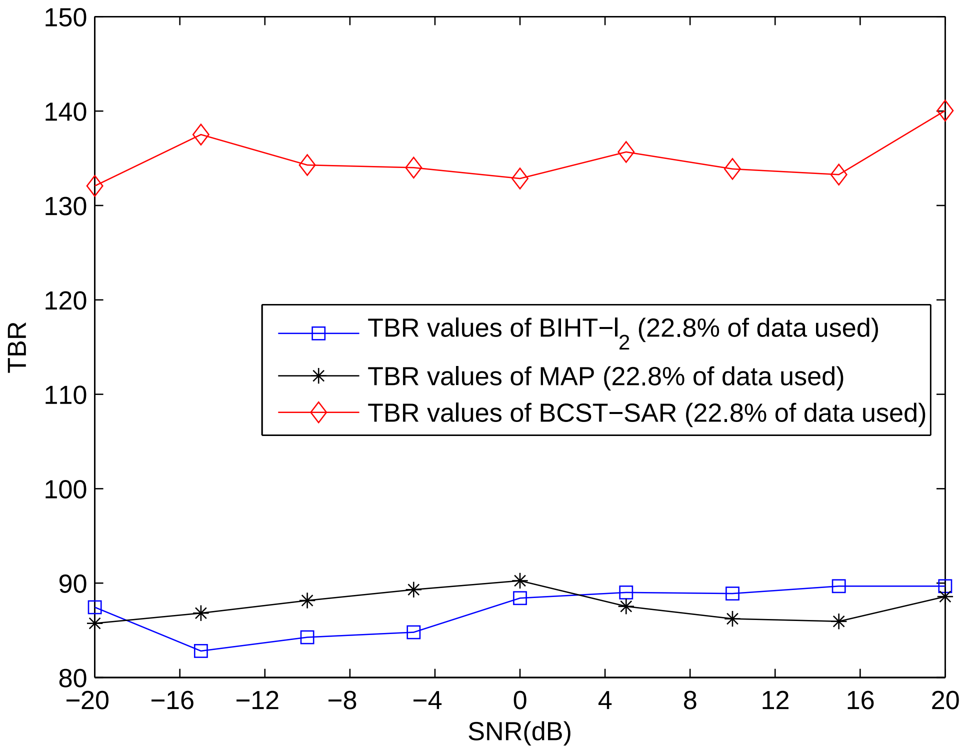

Figure 4.9 TBR values of the SIR-C/X-SAR image experiment using BIHT-ℓ_2, MAP and BCST-SAR under different SNR levels.

BIHT-ℓ_2 and MAP methods are very precise in determining the locations of the targets on SAR scene and the edges of the targets appear very clearly. However, the inner points of the targets disappear. The targets in SAR scene are recovered more precisely by the proposed BCST-SAR approach because BCST-SAR uses time-varying thresholding for 1-bit quantization and the amplitude values of the recovered SAR signal are more accurate.

Performance metrics are given in Table 4.3 to test how BCST-SAR, MAP and BIHT-ℓ_2 result in at different measurement percentages. As we can see from the results in Table 4.3, BCST-SAR outperforms BIHT-ℓ_2, and MAP.

Table 4.3 Performance metrics for the reconstructed images of a SAR data extracted from a real SIR-C/X-SAR image by BIHT-ℓ_2, MAP and BCST-SAR at different levels of measurement percentages ($SNR = 20\ dB$).

Measurement Percentage		MSE	TBR
7.6%	BIHT-ℓ_2	0.0032	88.3606
	MAP	0.0032	140.1953
	BCST-SAR	0.0032	172.5648
13.7%	BIHT-ℓ_2	0.0032	90.1975
	MAP	0.0030	95.8357
	BCST-SAR	0.0028	139.2523
22.8%	BIHT-ℓ_2	0.0032	89.6689
	MAP	0.0029	92.5628
	BCST-SAR	0.0026	140.0332
37%	BIHT-ℓ_2	0.0032	89.8096
	MAP	0.0029	93.7163
	BCST-SAR	0.0027	134.7164

For the proposed BCST-SAR algorithm, stopping criterion is designed as the relative cost function value $\frac{|g^{k+1}-g^k|}{g^k}$ error below 10^{-5}, where the objective function g is described in (3.14)[33, 36].

4.5 Parameter Selection of BCST-SAR Algorithm

The regularization parameter τ is hand-tuned for our simulations. However, the parameter selection techniques that are mentioned in [61] can be adapted to our problem. On the other hand, parameter μ can be varied at each iteration in ADMM algorithm for faster convergence[50]. However, we pick $\mu = 1$ in our simulations for getting better quality reconstructed SAR images.

Simulations have been performed with two different radar scenes to see how the change of parameters τ and μ affect the convergence speed of our algorithm and the reconstructed SAR image. For these simulations, a synthetically produced radar scene with a certain geometric shape and a small part of data extracted from a SIR-C/X-SAR image have been used. In the first, we increased τ while keeping $\mu = 1$. We have observed that the proposed approach finds sparser solutions as expected but the computation time of the algorithm is increased. The results can be seen in Figures 4.10, 4.11, 4.14, 4.15. In the second simulation, we keep τ constant and increase the value of ADMM parameter μ. In this case, the convergence speed rises but the reconstructed images are distorted. For this reason, we pick $\mu = 1$ for simulations in our work.

The regularisation parameter τ can be chosen automatically in real applications by using the techniques which are explained in [61]. L-curve among the defined techniques can be adapted to our algorithm since it necessitates less computational effort. For parameter μ, varying it at each iteration can be solution for faster convergence. But selecting the value of μ automatically for real applications remains an open question. On the other hand, $\mu = \tau/10$ is suggested as a good rule of thumb in [36].

In order to visually identify the convergence speed of BCST-SAR algorithm depending on τ and μ changing, the gradual development of objective function is plotted against number of iterations in Figures 4.12, 4.13, 4.16, 4.17. The smaller τ value, the faster the convergence speed is. The opposite is true for ADMM parameter μ.

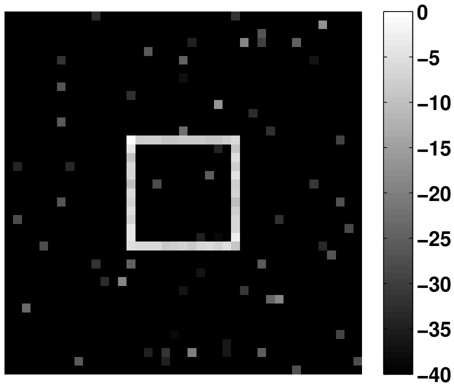

(a)
$\tau = 10,\ \mu = 1,\ t = 11.679267\ s$

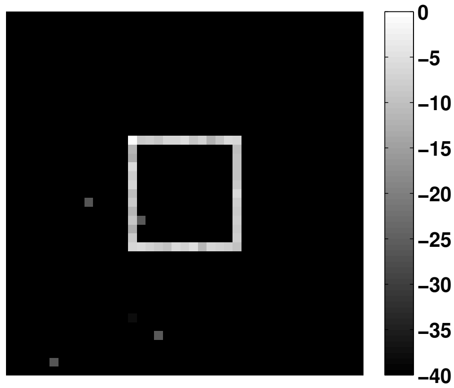

(b)
$\tau = 20,\ \mu = 1,\ t = 18.653472\ s$

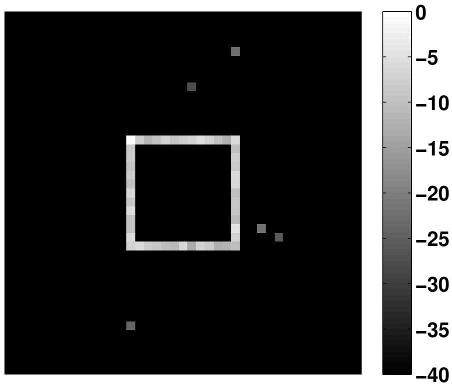

(c)
$\tau = 30,\ \mu = 1,\ t = 26.459116\ s$

Figure 4.10 The effect of choosing different τ values on the reconstructed certain geometry shape image and computation time.

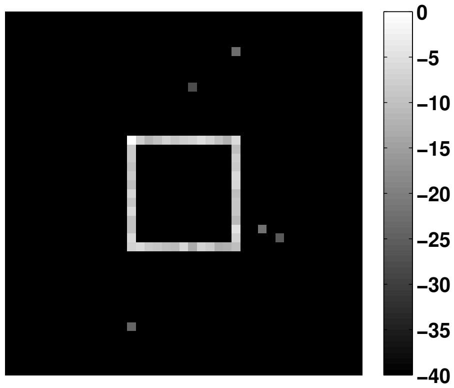

(a)
$\tau = 30,\ \mu = 1,\ t = 26.459116\ s$

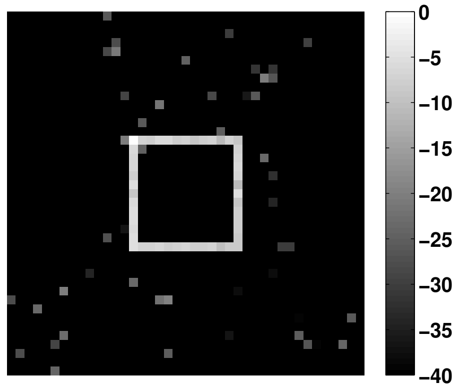

(b)
$\tau = 30,\ \mu = 5,\ t = 15.813535\ s$

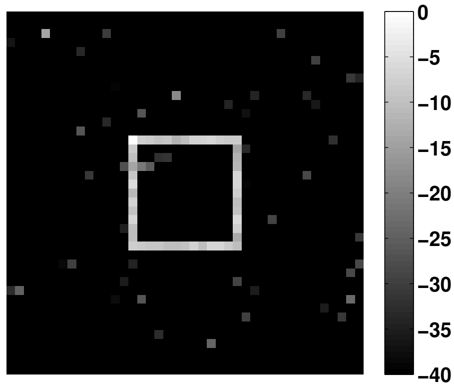

(c)
$\tau = 30,\ \mu = 10,\ t = 8.452067\ s$

Figure 4.11 The effect of choosing different μ values on the reconstructed certain geometry shape image and computation time.

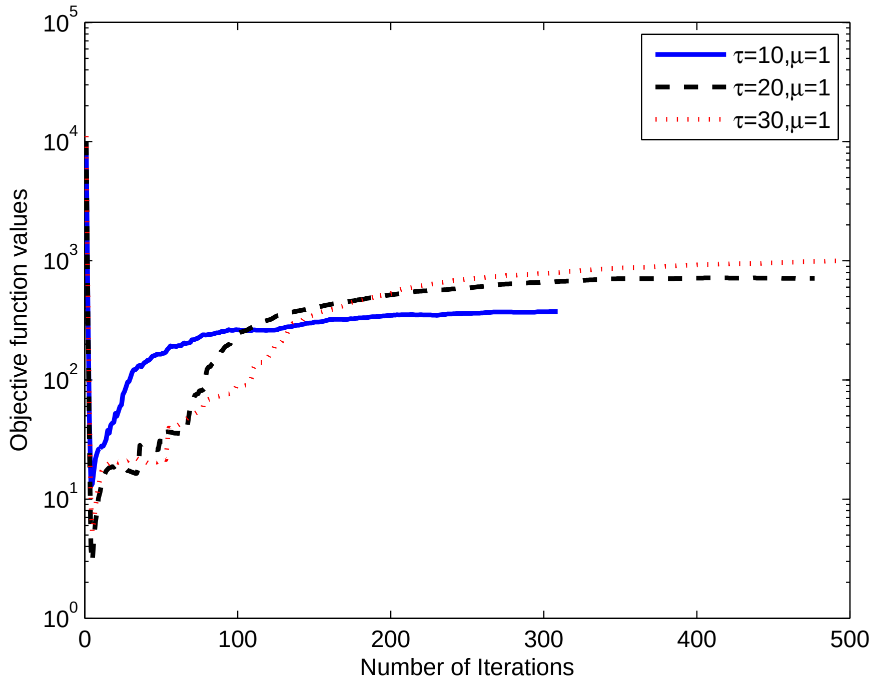

Figure 4.12 Objective function values versus number of iterations for certain geometry shape radar scene while τ changing.

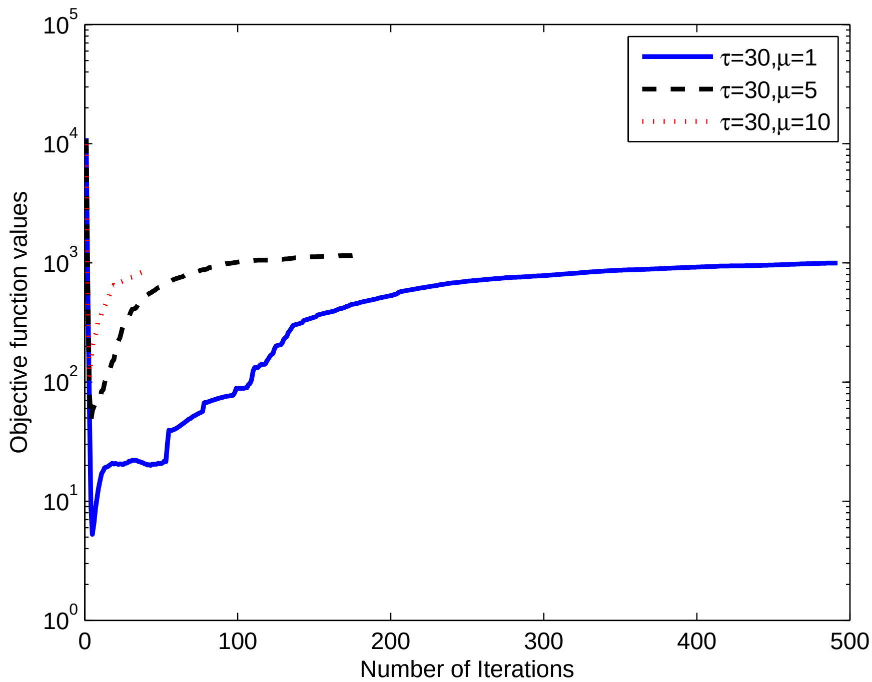

Figure 4.13 Objective function values versus number of iterations for certain geometry shape radar scene while μ changing.

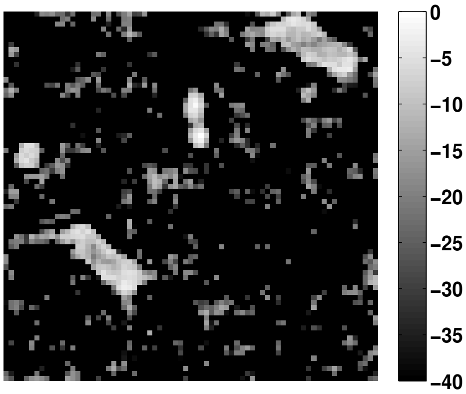

(a)
$\tau = 30$, $\mu = 1$, $t = 369.380387\ s$

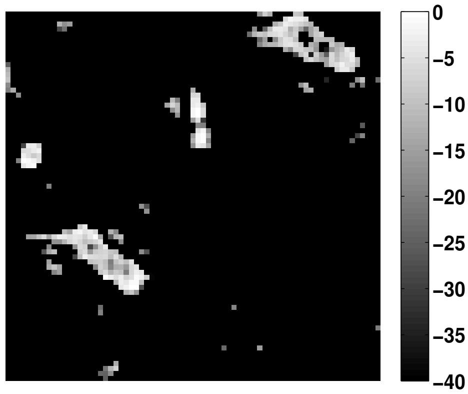

(b)
$\tau = 80$, $\mu = 1$, $t = 513.321095\ s$

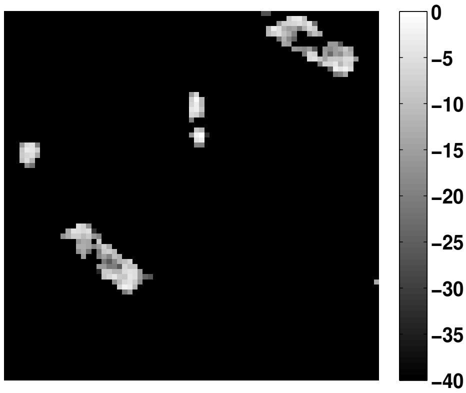

(c)
$\tau = 130$, $\mu = 1$, $t = 519.793817\ s$

Figure 4.14 The effect of choosing different τ values on the reconstructed SIR-C/X-SAR image and computation time.

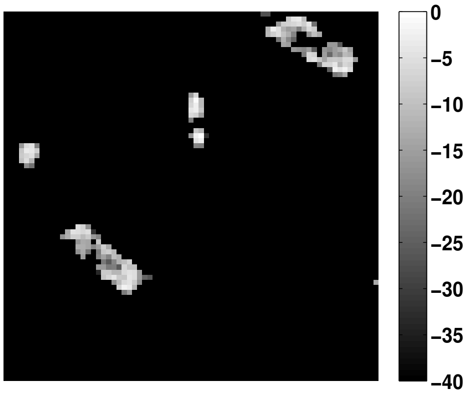

(a)
$\tau = 130$, $\mu = 1$, $t = 519.793817\ s$

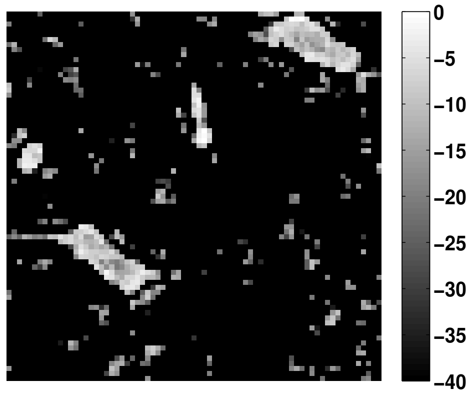

(b)
$\tau = 130$, $\mu = 5$, $t = 350.930311\ s$

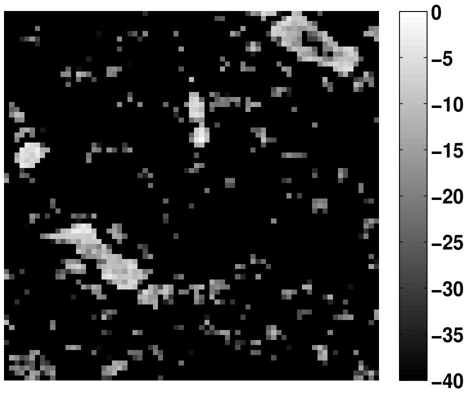

(c)
$\tau = 130$, $\mu = 10$, $t = 314.711162\ s$

Figure 4.15 The effect of choosing different μ values on the reconstructed SIR-C/X-SAR image and computation time.

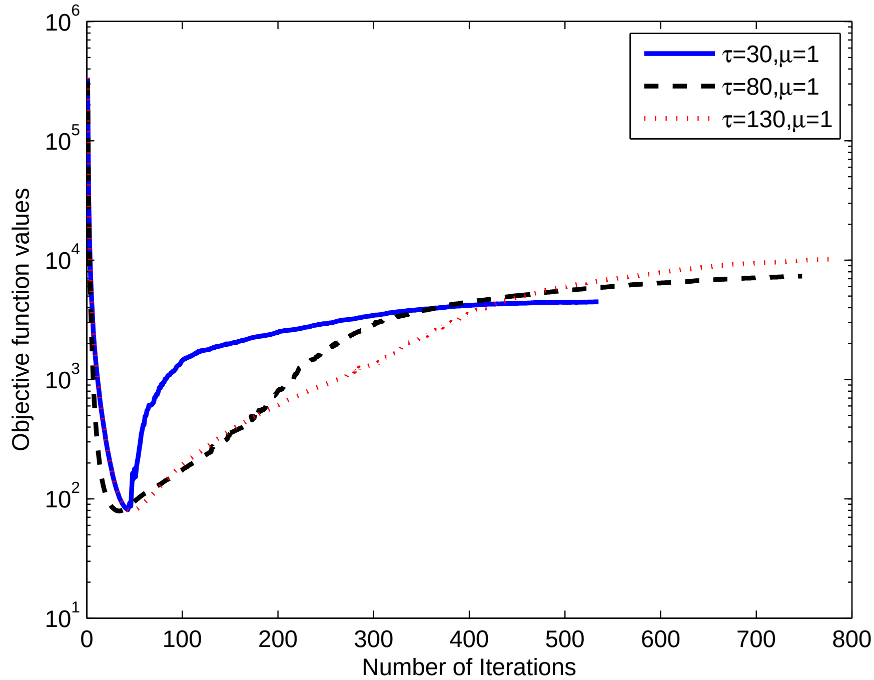

Figure 4.16 Objective function values versus number of iterations for SIR-C/X-SAR image while τ changing.

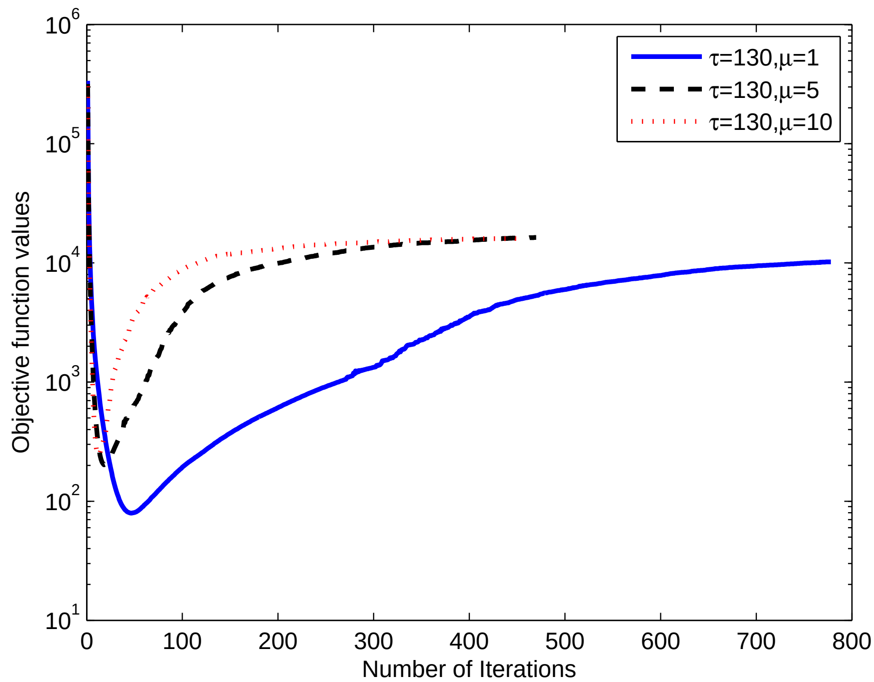

Figure 4.17 Objective function values versus number of iterations for SIR-C/X-SAR image while μ changing.

4.6 Run Time Comparisons of State-of-the-art Algorithms

All experiments have been implemented on a workstation equipped with Intel Xeon 3.50 GHz processor, with 24 GB of RAM and running on Windows 7. The run time comparisons of different techniques are depicted in Table 4.4. We conclude from Table 4.4 that the proposed BCST-SAR algorithm is clearly faster than MAP approach. In addition, BCST-SAR has the computational efficiency as much as a greedy BIHT-ℓ_2 algorithm, which is popular with computational efficiency.

Table 4.4 Run time comparisons of different state-of-the-art methods for 1-bit CS SAR imaging.

Algorithms	1st Exp.(s)	2nd Exp.(s)	3rd Exp.(s)
BIHT-ℓ_2	1.11	27.97	448.98
MAP	45.07	1177.29	10955.38
BCST-SAR	2.60	28.07	522.59

CHAPTER 5

CONCLUSIONS AND FUTURE WORK

5.1 Conclusions

1-bit quantization in SAR imaging provides significant benefits by increasing the speed of ADC and reducing the storage memory. 1-bit MF method used for recovering image from 1-bit quantized SAR data includes ghost targets and high side-lobes. In this study, we have introduced a compressive SAR imaging of sparse scenes with 1-bit quantization of received noisy thresholded measurements. The proposed method to solve the resulting optimization problem is based on ADMM which is computationally efficient and easy to implement. With BCST-SAR method, which uses time-varying thresholds in 1-bit quantization, the amplitudes or norm of the images are more accurate. The results of experiments with synthetic and real SAR images demonstrate that the effectiveness of the proposed approach. In these performed experiments, BCST-SAR succeeds in removing ghost targets and suppressing noisy background.

BCST-SAR has been compared with classical 1-bit MF and state-of-the-art 1-bit CS methods. In these comparisons, BCST-SAR provides better SAR image reconstructions than BIHT-ℓ_2, MAP and the conventional 1-bit MF in terms of performance metrics. In simulations with synthetic and real SAR images, BCST-SAR algorithm has produced lower MSE values. Besides, it has yielded higher TBR values than BIHT-ℓ_2 and MAP algorithms. In addition to these simulations, the amplitudes of the images obtained from BCST-SAR algorithm are more accurate, as shown in scene sparsity versus $pSNR$ graph. On the other hand, in order to show the novelty of the proposed approach, the run time comparisons of state-of-the-art BIHT-ℓ_2, MAP and BCST-SAR methods have been given. It has been shown from this comparison that BCST-SAR is as fast as the greedy BIHT-ℓ_2 algorithm which is computationally efficient. It should be considered that the proposed scheme may be an alternative to other methods used in 1-bit CS SAR imaging.

5.2 Future Work

It should be emphasized that BCST-SAR has been only applied to scenes that are sparse in the image domain, not for complex SAR images. The application of it to complex SAR images is the subject of another study.

Elimination of phase errors caused by motion-induced uncertainties and other modelling imperfections in 1-bit CS SAR imaging will be dealt with in our future work to complement the presented work in this dissertation.

In these all aforementioned methods, sign flips happen due to the noise in measurements. In next studies, algorithms which detect the positions where sign flips occur can be added to BCST-SAR method. In case detection technique is added to the current method, the results will be more precise.

In addition, L-curve among the defined techniques in [61] can be adapted to our proposed BCST-SAR method for determining the regularization parameter since it necessitates less computational effort. By means of L-curve, the algorithm can produce sparser scenes with less computational complexity.

REFERENCES

[1] Uğur, S. (2013). Novel methods for SAR imaging problems. PhD Thesis, Bilkent University, Ankara.

[2] NASA. National Aeronautics and Space Administration. SIR-C/X-SAR Image
https://photojournal.jpl.nasa.gov/catalog/pia01843, November 2017.

[3] Wu, C., Liu, K. Y., Jin, M. J. (1982). Modelling and a correlation algorithm for spaceborne SAR signals. *IEEE Transactions on Aerospace and Electronic Systems.* **AES-18**, 563-574.

[4] Raney, R. K., Runge, H., Bamler, R., Cumming, I. G., Wong, F. H. (1994). Precision SAR processing using chirp scaling. *IEEE Transactions on Geoscience and Remote Sensing.* **32**, 786-799.

[5] Cafforio, C., Prati, C., Roca, F. (1991). SAR data focusing using seismic migration techniques. *IEEE Transactions on Aerospace and Electronic Systems.* **27**, 194-207.

[6] Carrara WG, Goodman RS, Majewski RM. 1995. Spotlight synthetic aperture radar: signal processing algorithms. Boston, London: Artech House Inc.

[7] Munson, Jr. D. C., O'Brien, J. C., Jenkins, W. K. (1983). A tomographic formulation of spotlight-mode synthetic aperture radar. *Proceedings of IEEE.* **71**, 971-925.

[8] LeRoy, A. G., Linda, J. M. (2010). SAR image formation toolbox for MATLAB. Algorithms for Synthetic Aperture Radar Imagery XVII. Proceedings of SPIE 7699, pp.7699 - 7699 - 13.

[9] Franceschetti, G., Pascazio, V., Schirinzi, G. (1991). Processing of signum coded SAR signal: theory and experiments. *IEE Proceedings F - Radar and Signal Processing.* **138**, 192-198.

[10] Alberti, G., Franceschetti, G., Schirinzi, G., Pascazio, V. (1991). Time-domain convolution of one-bit coded radar signals. *IEE Proceedings F - Radar and Signal Processing.* **138**, 438-444.

[11] Pascazio, V., Schirinzi, G. (1998). Synthetic aperture radar imaging by one bit coded signals. *Electronics and Communication Engineering Journal.* **10**, 17-28.

[12] Franceschetti, G., Merolla, S., Tesauro, M. (1999). Phase quantized SAR signal processing: theory and experiments. *IEEE Transactions on Aerospace and Electronic Systems.* **35**, 201-214.

[13] Dong, X., Zhang, Y. (2015). A MAP Approach for 1-Bit Compressive Sensing in Synthetic Aperture Radar Imaging. *IEEE Geoscience and Remote Sensing Letters.* **12**, 1237-1241.

[14] Zhou, C., Liu, F., Li, B., Hu, J., Lv, Y. (2016). A 1-bit compressive sensing approach for SAR imaging based on approximated observation. Eighth International Conference on Digital Image Processing (ICDIP 2016). Proceedings of SPIE 10033, pp.10033 - 10033 - 7.

[15] Donoho, D. L. (2006). Compressed sensing. *IEEE Transactions on Information Theory.* **52**, 1289-1306.

[16] Candès, E. J., Wakin, M. B. (2008). An introduction to compressive sampling. *IEEE Signal Processing Magazine.* **25**, 21-30.

[17] Baraniuk, R. G., Steeghs, P. (2007). Compressive radar imaging. 2007 IEEE Radar Conference. IEEE, pp.128-133.

[18] Patel, V. M., Easley, G. R., Healy, D. M., Chellappa, J. R. (2010). Compressed synthetic aperture radar. *IEEE Journal of Selected Topics in Signal Processing.* **4**, 244-254.

[19] Zymnis, A., Boyd, S., Candès, E. J. (2010). Compressed sensing with quantized measurements. *IEEE Signal Processing Letters.* **17**, 149-152.

[20] Boufounos, P. T., Baraniuk, R. G. (2008). 1-Bit compressive sensing. 2008 42nd Annual Conference on Information Sciences and Systems. IEEE, pp.16-21.

[21] Jacques, L., Laska, J. N., Boufounos, P. T., Baraniuk, R. G. (2013). Robust 1-bit compressive sensing via binary stable embeddings of sparse vectors. *IEEE Transactions on Information Theory.* **59**, 2082-2102.

[22] Boufounos, P. T. (2009). Greedy sparse signal reconstruction from sign measurements. 2009 Conference Record of the Forty-Third Asilomar Conference on Signals, Systems and Computers. IEEE, pp.1305-1309.

[23] Laska, J. N., Wen, Z., Yin, W., Baraniuk, R. G. (2011). Trust, but verify: fast and accurate signal recovery from 1-bit compressive measurements. *IEEE Transactions on Signal Processing.* **59**, 5289-5301.

[24] Yan, M., Yang, Y., Osher, S. (2012). Robust 1-bit compressive sensing using adaptive outlier pursuit. *IEEE Transactions on Signal Processing.* **60**, 3868-3875.

[25] Movahed, A., Panahi, A., Durisi, G. (2012). A robust RFPI-based 1-bit compressive sensing reconstruction algorithm. 2012 IEEE Information Theory Workshop. IEEE, pp. 567-571.

[26] Plan, Y., Vershynin, R. (2013). One-bit compressed sensing by linear programming. *Communications on Pure and Applied Mathematics.* **66**, 1275-1297.

[27] Plan, Y., Vershynin, R. (2013). Robust 1-bit compressed sensing and sparse logistic regression: A convex programming approach. *IEEE Transactions on Information Theory.* **59**, 482-494.

[28] Zhou, C., Zhang, Z., Liu, F. (2016). Robust 1-bit compressive sensing via variational Bayesian algorithm. *Digital Signal Processing.* **50**, 84-92.

[29] Fang, J., Shen, Y., Li, H., Ren, Z. (2014). Sparse signal recovery from one-bit quantized data: An iterative reweighted algorithm. *Signal Processing.* **102**, 201-206.

[30] Knudson, K., Saab, R., Ward, R. (2016). One-bit compressive sensing with norm estimation. *IEEE Transactions on Information Theory.* **62**, 2748-2758.

[31] Gianelli, C., Xu, L., Li, J., Stoica, P. (2016). One-bit compressive sampling with time-varying thresholds for sparse parameter estimation. 2016 IEEE Sensor Array and Multichannel Signal Processing Workshop (SAM). IEEE, pp.1-5.

[32] Gianelli, C., Xu, L., Li, J., Stoica, P. (2016). One-bit compressive sampling with time-varying thresholds: Maximum likelihood and the Cramér-Rao bound. 2016 50th Asilomar Conference on Signals, Systems and Computers. IEEE, pp.399-403.

[33] Qian, C., Li, J. (2017). ADMM for harmonic retrieval from one-bit sampling with time-varying thresholds. 2017 IEEE International Conference on Acoustics, Speech and Signal Processing (ICASSP). IEEE, pp.3699-3703.

[34] Li, J., Naghsh, M. M., Zahabi, S. J., Modarres-Hashemi, M. (2016). Compressive radar sensing via one-bit sampling with time-varying thresholds. 2016 50th Asilomar Conference on Signals, Systems and Computers. IEEE, pp.1164-1168.

[35] Zahabi, S. J., Naghsh, M. M., Modarres-Hashemi, M., Li, J. (2017). Compressive pulse-Doppler radar sensing via 1-bit sampling with time-varying threshold. 2017 IEEE International Conference on Acoustics, Speech and Signal Processing (ICASSP). IEEE, pp.3419-3423.

[36] Afonso, M. V., Bioucas-Dias, J. M., Figueiredo, M. A. T. (2010). Fast image recovery using variable splitting and constrained optimization. *IEEE Transactions on Image Processing.* **19**, 2345-2356.

[37] Güven, H.E., Güngör, A., Çetin, M. (2016). An Augmented lagrangian method for complex-valued compressed SAR imaging. *IEEE Transactions on Computational Imaging.* **2**, 235-250.

[38] Önhon, N.Ö. (2012). Joint sparsity-driven inversion and model error correction for SAR imaging. PhD Thesis, Sabancı University, İstanbul.

[39] Cetin, M., Karl, W. C. (2001). Feature-enhanced synthetic aperture radar image formation based on nonquadratic regularization. *IEEE Transactions on Image Processing.* **10**, 623-631.

[40] Xu, J., Pi, Y., Cao, Z. (2012). Bayesian compressive sensing in synthetic aperture radar imaging. *IET Radar, Sonar and Navigation.* **6**, 2-8.

[41] Jakowatz CVJ, Wahl DE, Eichel PH, Ghiglia DC, Thompson PA. 1996. Spotlight-mode synthetic aperture radar: a signal processing approach. Albuquerque, New Mexico: Springer.

[42] Kak AC, Slaney M. 1988. Principles of computerized tomographic imaging. New York: IEEE Press.

[43] Uğur, S., Arıkan, O. (2012). SAR image reconstruction and autofocus by compressed sensing. *Digital Signal Processing.* **22**, 923-932.

[44] Uğur, S., Arıkan, O., Gürbüz, A.C. (2015). SAR image reconstruction by expectation maximization based matching pursuit. *Digital Signal Processing.* **37**, 75-84.

[45] Donoho, D.L., Stark, P.B. (1989). Uncertainty principles and signal recovery. *SIAM J. Appl. Math.* **49**, 906-931.

[46] Tropp, J.A., Gilbert, A.C. (2007). Signal recovery from random measurements via orthogonal matching pursuit. *IEEE Transactions on Information Theory.* **53**, 4655-4666.

[47] Yin, W., Osher, S., Goldfarb, D., Darbon, J. (2008). Bregman iterative algorithms for ℓ_1-minimization with applications to compressed sensing. *SIAM J. Imaging Sci..* **1**, 143-168.

[48] Vandenberg, E., Friedlander, M.P. (2008). Probing the Pareto frontier for Basis Pursuit solutions. *SIAM J. Sci. Comput..* **31**, 890-912.

[49] Candès, E. J., Romberg, J.K., Tao, T. (2006). Stable signal recovery from incomplete and inaccurate measurements. *Communications on Pure and Applied Mathematics.* **59**, 1207-1223.

[50] Boyd, S., Parikh, N., Chu, E., Peleato, B., Eckstein, J. (2011). Distributed optimization and statistical learning via the alternating direction method of multipliers. *Foundations and Trends® in Machine Learning.* **3**, 1–122.

[51] Rilling, G., Davies, M., Mulgrew, B. (2009). Compressed sensing based compression of SAR raw data. Signal Processing with Adaptive Sparse Structured Representations (SPARS'09). HAL-Inria, pp.1-6.

[52] Wang, Y., Yang, J., Yin, W., Zhang, Y. (2008). A new alternating minimization algorithm for total variation image reconstruction. *SIAM J. Imaging Sci..* **1**, 248–272.

[53] Bioucas-Dias, J.M., Figueiredo, M.A.T. (2008). An iterative algorithm for linear inverse problems with compound regularizers. 2008 15th IEEE International Conference on Image Processing. IEEE, pp.685-688.

[54] Bertsekas DP. 2015. Convex optimization algorithms. Belmont, Massachusetts: Athena Scientific.

[55] Afonso, M.V., Bioucas-Dias, J.M., Figueiredo, M.A.T. (2011). An augmented Lagrangian approach to the constrained optimization formulation of imaging inverse problems. *IEEE Transactions on Image Processing*. **20**, 681-695.

[56] Güven, H.E., Güngör, A., Çetin, M. (2015). An Augmented Lagrangian method for image reconstruction with multiple features. 2015 IEEE International Conference on Image Processing (ICIP). IEEE, pp. 4175-4179.

[57] Eckstein, J., Bertsekas, D.P. (1992). On the Douglas—Rachford splitting method and the proximal point algorithm for maximal monotone operators. *Mathematical Programming*. **55**, 293-318.

[58] Laurent Jacques' Homepage Main / BIHT Demo browse `https://perso.uclouvain.be/laurent.jacques/BIHTDemo`, November 2017.

[59] Hasankhan, M.J., Samadi, S., Çetin, M. (2017). Sparse representation-based algorithm for joint SAR image formation and autofocus. *Signal, Image and Video Processing*. **11**, 589–596.

[60] Cetin, M. (2001). Feature-enhanced synthetic aperture radar imaging. PhD dissertation, College of Engineering, Boston University, Boston.

[61] Batu, O., Çetin, M. (2011). Parameter selection in sparsity-driven SAR imaging. *IEEE Transactions on Aerospace and Electronic Systems*. **47**, 3040-3050.

APPENDIX A

DERIVATION OF ADMM X-ITERATION

In this appendix, it is explained how to obtain (3.34) from (3.30). When ADMM is applied to 1-bit CS SAR imaging problem quantized with time-varying thresholds, the following x-iteration acquired.

$$\mathbf{x}^{k+1} = \arg\min_{\mathbf{x}\in\mathbb{R}^{2N}} \|\mathbf{A}\mathbf{x} - \mathbf{y}\odot\mathbf{b} - \mathbf{h}\|_2^2 + \frac{\mu}{2}\|\mathbf{x} - \mathbf{v}^k - \mathbf{d}^k\|_2^2 \tag{A.1}$$

First, let's name the function to be minimized and can be re-written clearly as follows:

$$p(\mathbf{x}) = \|\mathbf{A}\mathbf{x} - \mathbf{y}\odot\mathbf{b} - \mathbf{h}\|_2^2 + \frac{\mu}{2}\|\mathbf{x} - \mathbf{v}^k - \mathbf{d}^k\|_2^2 \tag{A.2}$$

$$\begin{aligned} p(\mathbf{x}) =& (\mathbf{A}\mathbf{x})^H(\mathbf{A}\mathbf{x}) - (\mathbf{A}\mathbf{x})^H(\mathbf{y}\odot\mathbf{b}) - (\mathbf{A}\mathbf{x})^H\mathbf{h} - (\mathbf{y}\odot\mathbf{b})^H(\mathbf{A}\mathbf{x}) \\ &+ (\mathbf{y}\odot\mathbf{b})^H(\mathbf{y}\odot\mathbf{b}) + (\mathbf{y}\odot\mathbf{b})^H\mathbf{h} - \mathbf{h}^H(\mathbf{A}\mathbf{x}) + \mathbf{h}^H(\mathbf{y}\odot\mathbf{b}) + \mathbf{h}^H\mathbf{h} \\ &+ \frac{\mu}{2}(\mathbf{x}^H\mathbf{x} - \mathbf{x}^H\mathbf{v} - \mathbf{x}^H\mathbf{d} - \mathbf{v}^H\mathbf{x} + \mathbf{v}^H\mathbf{v} + \mathbf{v}^H\mathbf{d} - \mathbf{d}^H\mathbf{x} + \mathbf{d}^H\mathbf{v} + \mathbf{d}^H\mathbf{d}) \end{aligned} \tag{A.3}$$

The gradient of $p(\mathbf{x})$ is given by

$$\begin{aligned} \nabla p(\mathbf{x}) =& 2\mathbf{x}^H\mathbf{A}^H\mathbf{A} - \mathbf{A}^H(\mathbf{y}\odot\mathbf{b}) - \mathbf{A}^H\mathbf{h} - (\mathbf{y}\odot\mathbf{b})^H\mathbf{A} - \mathbf{h}^H\mathbf{A} \\ &+ \frac{\mu}{2}(2\mathbf{x}^H - \mathbf{v} - \mathbf{d} - \mathbf{v}^H - \mathbf{d}^H) \end{aligned} \tag{A.4}$$

If the gradient of $p(\mathbf{x})$ is equated to 0, the following expression occurs

$$0 = \mathbf{x}^H\mathbf{A}^H\mathbf{A} - \mathbf{A}^H(\mathbf{y}\odot\mathbf{b}) - \mathbf{A}^H\mathbf{h} + \mu\mathbf{x}^H - \mu\mathbf{v} - \mu\mathbf{d} \tag{A.5}$$

The following expression takes place when the statements with $\mathbf{x}$ are aggregated on one side of the equation.

$$(\mathbf{A}^H\mathbf{A} + \mu\mathbf{I})\mathbf{x} = \mathbf{A}^H(\mathbf{y} \odot \mathbf{b} + \mathbf{h}) + \mu(\mathbf{v} + \mathbf{d}) \tag{A.6}$$

Finally, we get the following $\mathbf{x}$-iteration statement:

$$\mathbf{x} = (\mathbf{A}^H\mathbf{A} + \mu\mathbf{I})^{-1}[\mathbf{A}^H(\mathbf{y} \odot \mathbf{b} + \mathbf{h}) + \mu(\mathbf{v} + \mathbf{d})] \tag{A.7}$$

APPENDIX B

CODE FOR BCST-SAR ALGORITHM

```
function [v, temp] = BCST_SAR(A, b, h, tau, mu, alpha)
% BCST-SAR Algorithm for 1-bit CS SAR Imaging
% BCST-SAR solves the following problem via Variable Splitting
% and ADMM
% min ||Ax-y.*b-h||_2^2 + \tau*sum_(i=1)^N (x_i^2+x_(i+N)^2)

t_start = tic;

flag = 0;
max_itr = 1000;
abs_tol = 1e-4;
rel_tol = 1e-2;
tol = 1e-5;
[m, n] = size(A);

x = zeros(n,1);
v = zeros(n,1);
d = zeros(n,1);
y = ones(m,1);
cost_old = 1e-6;

% factor the A matrix term
[L U] = factorization(A, mu);

if ~flag
fprintf('%3s\t%10s\t%10s\t%10s\t%10s\t%10s\n', 'iter', ...
'r norm', 'eps pri', 's norm', 'objective', 'relative cost');
end
```

```
for k = 1:max_itr

% x-update
q = A'*(b.*y + h) + mu*(v + d);     % temporary value
if( m >= n )
x = U \ (L \ q);
else
x = q/mu - (A'*(U \ ( L \ (A*q) )))/mu^2;
end

y = abs(A*x - h);
% v-update with relaxation
vold = v;
x_hat = alpha*x + (1 - alpha)*vold;
v = shrinkage(x_hat - d, tau/mu);

% d-update
d = d - (x_hat - v);

% diagnostics, reporting, termination checks
temp.objval(k)  = objective(A, b, y, h, tau, x, v);
cost = temp.objval(k);
rel_cost = abs(cost - cost_old)/cost_old;

temp.r_norm(k)  = norm(x - v);
temp.s_norm(k)  = norm(-mu*(v - vold));

temp.eps_pri(k) = sqrt(n)*abs_tol + rel_tol*max(norm(x), ...
norm(-v));
temp.eps_dual(k)= sqrt(n)*abs_tol + rel_tol*norm(mu*d);

if ~flag
fprintf('%3d\t%10.4f\t%10.4f\t%10.4f\t%10.2f\t%10.6f\n', ...
k, temp.r_norm(k), temp.eps_pri(k), ...
temp.s_norm(k), temp.objval(k), rel_cost);
end

if (rel_cost < tol)
break;
```

```
end

cost_old = cost;
end

if ~flag
toc(t_start);
end
end


function [L U] = factorization(A, mu)
[m, n] = size(A);
% cholesky factorization is used
if ( m >= n )
L = chol( A'*A + mu*speye(n), 'lower' );
else
L = chol( speye(m) + 1/mu*(A*A'), 'lower' );
end

% upper or lower triangular
L = sparse(L);
U = sparse(L');
end


function p = objective(A, b, y, h, tau, x, v)
n= length(v);
for i = 1:n/2
t(i)= sqrt(v(i)^2 + v(i + n/2)^2);
end
p = ( 1/2*sum((A*x - b.*y - h).^2) + tau*sum(t));
end



function z = shrinkage(x, kappa)

n = length(x);
for i = 1:n/2
z(i,1) = max( 0, sqrt(x(i)^2 + x(i + n/2)^2) - kappa ) * ...
```

```
(x(i)/sqrt(x(i)^2 + x(i + n/2)^2));
end
for i = n/2+1:n
z(i,1) = max( 0, sqrt(x(i)^2 + x(i - n/2)^2) - kappa ) * ...
(x(i)/sqrt(x(i)^2 + x(i - n/2)^2));
end
end
```

APPENDIX C

CODE FOR MAP ALGORITHM

```
function [x, temp] = OneBitCS_SAR_MAP(A, q, lambda)

t_start = tic;

flag    = 0;
max_itr = 1000;
tol = 1e-3;

[m, n] = size(A);

alpha = 1;
Beta = 1/(norm(A)^2);
y = zeros(m,1);
x = (A'*y)/(norm(A)^2);
x_bar = x;

if ~flag
fprintf('%3s\t%10s\t%10s\n', 'iter', 'x norm', 'objective');
end

for k = 1:max_itr

y_pri = y + Beta*A*x_bar;
%y_pri/Beta update
w = P_Beta_inv_F(q, y_pri, Beta);
y = y_pri - Beta*w;
x_old = x;
x_pri = x_old - alpha*A'*y;
x = shrinkage(x_pri, alpha*lambda);
```

```
x_bar = 2*x - x_old;


% diagnostics, reporting, termination checks
temp.objval(k)  = objective(A, q, x, lambda);
temp.x_norm(k)  = norm(x - x_old)/norm(x_old);


if ~flag
fprintf('%3d\t%10.4f\t%10.2f\n', k, temp.x_norm(k),...
temp.objval(k));
end


if temp.x_norm(k) < tol
break;
end
end

if ~flag
toc(t_start);
end
end


function u = P_Beta_inv_F(q, y_pri, B)

alpha = 0.1;
BETA  = 0.5;
tol = 1e-5;
max_itr = 50;

m = length(y_pri);

u = rand(m,1);

f = @(w) (-1/B * sum(log(normcdf(q.*w)))...
 + 1/2*norm(w - y_pri/B).^2);
for iter = 1:max_itr
fu = f(u);
```

```
g = (-1/(B*sqrt(2*pi)))*q.*(exp(-0.5*(q.*u).^2))...
    ./(normcdf(q.*u)) + u - y_pri/B;
h = (-1/(B*sqrt(2*pi)))*q.*((-(q.^2).*u).*...
exp(-0.5*(q.*u).^2).*normcdf(q.*u) - (1/(sqrt(2*pi)))...
*exp(-(q.*u).^2).*q)./((normcdf(q.*u)).^2)+ ones(m,1);
H = diag(h);
du = -H\g;   % Newton step
dfu = g'*du; % Newton decrement
if abs(dfu) < tol
break;
end
% backtracking
t = 1;
while f(u + t*du) > fu + alpha*t*dfu
t = BETA*t;
end
u = u + t*du;
end
end


function obj = objective(A, q, x, lambda)

n = length(x);
obj = -sum(log(normcdf(diag(q)*A*x)))...
 + lambda*sum((x(1:n/2).^2+(x(n/2+1:n)).^2).^1/2);

end
```

Publications

Demir, M., Koraşlı, C. (2014). Statistical approach for determining impulse breakdown voltage distribution under DC sweep voltage. *Turkish Journal of Electrical Engineering and Computer Sciences*. **22**, 12-24.

Demir, M., Erçelebi, E. (2018). One-bit compressive sensing with time-varying thresholds in synthetic aperture radar imaging. *IET Radar, Sonar and Navigation*. **12**, 1517-1526.

CIRRICULUM VITAE

PERSONAL INFORMATION

Surname, Name : DEMİR, Mehmet

Nationality : Turkish (TC)

Date and Place of Birth : 25 August 1986, Gaziantep/Turkey

Office Phone : +90 342 317 2153

email : mehmetdemir@gantep.edu.tr

EDUCATION

Degree	Institution	Year of Graduation
MSc	Gaziantep University	2012
BSc	Gaziantep University	2009

WORK EXPERIENCE

Year	Place	Enrollment
2009-present	Gaziantep University	Research Assistant